ISSN 1331-7210

Engineering Power

BULLETIN OF THE CROATIAN ACADEMY OF ENGINEERING Vol. 14(1) 2019

EDITOR-IN-CHIEF'S WORD

In its 26 years of existence the Croatian Academy of Engineering has always striven to publish the results of its distinguished members in professional and scientific research fields, which also gives an insight into the relevant achievements of engineering sciences in Croatia.

In order that this insight is more widely visible, in its Bulletin Engineering Power the Academy periodically presents some of these results that seem to be interesting, which is also confirmed by this issue.

Therefore, I believe that the articles prepared by our regular member Zdenko Tonković with his associates present good information and benefit to everyone who closely pursues the field of mechanical engineering.

Editor-in-Chief
Vladimir Andročec, President of the Croatian Academy of Engineering

EDITOR'S WORD

Dear readers,

Production and application of new advanced materials are, beyond any doubt, one of the most important fields in modern science and technology.

In this edition of Academy's Bulletin Engineering Power we are focusing on the related research area: structural analysis of such materials based on numerical modelling and development of the pertinent computational simulation tools.

The Guest-Editor of this issue is Zdenko Tonković, Member of the Academy and Professor at the Faculty of Mechanical Engineering and Naval Architecture, University of Zagreb, who is presenting part of the activities of the Faculty's Laboratory for Numerical Mechanics.

Editor
Zdravko Terze, Vice-President of the Croatian Academy of Engineering

FOREWORD

New demands on safety, reliability, maintainability, efficiency and optimal control, together with the applications of new materials and new production technologies, can only be realized by using methods of advanced structural analysis and more realistic description of material behaviour. Therein, material heterogeneity plays a major role, because almost all materials are heterogeneous and anisotropic due to their natural structure, particularly on the microscopic scale, or as the result of manufacturing procedure. The crack initiation and propagation in heterogeneous material are under the great influence of the microstructure and properties of its constituents and defects as well as the residual stresses due to the various manufacturing processes, such as welding. Therefore, in order to predict the failure of engineering materials and structures for the purpose of structural integrity assessment, an accurate and efficient analysis on the microlevel is unavoidable. As in many other cases, numerical simulations are widely used to complement or substitute much more expensive experiments.

The papers listed below represent a part of the scientific research in the above-mentioned fields of the members of the Laboratory for Numerical Mechanics at the Faculty of Mechanical Engineering and Naval Architecture, University of Zagreb and their associates from the Faculty and industry. The studies have been carried out within the frame of the projects approved by the Croatian Science Foundation and the European Union through the Science and Innovation Investment Fund Grant Scheme, as well as the project funded by the Alexander von Humboldt foundation from Germany. The first paper deals with the numerical modelling of fracture phenomena occurring in real microstructures of heterogeneous materials. The arbitrary heterogenous geometry based on a microstructure of nodular cast iron is analysed with the phase-field method which, in the past few years, has emerged as a very *powerful* simulation *tool to* predict complex crack patterns even in three-dimensional settings. The second paper presents the multiscale modelling of heterogeneous materials, where the macroscopic properties are being determined by the homogenization process acting on an effective, homogenized sample of material microstructure called representative volume element. Multiscale modelling has attracted increasing interest in past years not only in the scientific community but also in the industrial sector due to the recent dramatic increase in computational power, the experimental capabilities to provide material properties down to the atomic level, and the development of advanced methods, such as computational homogenization, that admit multiple length scales. The last paper presents an efficient finite element procedure for the prediction of welding-induced residual stresses and distortions in engineering structures. The numerical simulation of thick steel plates welding using new high-productive buried arc technology is performed and experimentally validated using a fully automated welding process.

Guest-Editor
Zdenko Tonković, University of Zagreb, Faculty of Mechanical Engineering and Naval Architecture

CONTENT

Karlo Seleš[1], Zdenko Tonković[1], Ante Jurčević[1], Jurica Sorić[1]

Numerical Modelling of Fracture Processes at the Microstructural level of Heterogeneous Materials

[1]Faculty of Mechanical Engineering and Naval Architecture, University of Zagreb, Zagreb, Croatia

Abstract

The prediction of crack propagation at the microstructural level of heterogeneous material, as is the case with the nodular cast iron, can be a very demanding problem. Lately, the phase-field approach to fracture has been shown a strong potential in modelling such complex crack behavior in a smeared-crack manner. In this work, the phase-field staggered residual norm based stopping criterion, recently developed by the authors, was utilized for the numerical simulation of the crack propagation within the heterogeneous microstructural geometry. The geometries were based on the metallographic images of the nodular cast iron with the graphite nodules considered as porosities. The proposed solution strategy is able to recover the complicated crack nucleation and propagation phenomena within the complex microstructural topology.

***Keywords**: heterogeneous materials, phase-field fracture modelling, staggered algorithm, Abaqus, crack initiation and propagation.*

1. Introduction

An accurate deformation response analysis of the heterogeneous materials often demands a precise modelling at both macroscopic and microscopic scales. The nodular cast iron is a good example of the material with highly heterogeneous microstructure consisting of graphite nodules placed inside a ferritic or a pearlitic matrix. However, not only the volume fraction and the material properties of the microstructural constituents, but also their size, shape and spatial distribution has an important influence on the macroscopic material behavior, as was presented in [1]. The experimental observations of the ductile nodular cast iron EN-GJS-400-18-LT mechanical behavior with emphasis on its material microstructure, have been well described in the previous works of the authors' research team [2, 3]. The cracked specimen with exposed nodular cast iron microstructure is presented in Fig. 1 where it can be seen how the crack is directed towards the graphite nodule which then acts as a barrier for further crack propagation. This is part of the reason why the nodular cast iron has great material fatigue properties and is often used in engineering practice for the design of structural components subjected to cyclic loads.

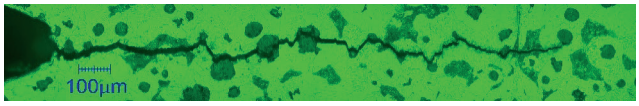

Fig. 1. Microstructural crack exposure [3]

Such cracking behavior within the heterogeneous microstructure often consists of complex cracking mechanisms such as crack initiation and propagation accompanied with the branching and merging of the crack paths. As a consequence, numerical modelling of fracture processes in heterogeneous microstructure poses an important and *challenging problem*. Accordingly, different numerical approaches and methods have been proposed for material fracture modelling. Often used numerical methods, which can be classified as the discrete crack interface methods for material fracture, introduce crack as a geometric discontinuity within the finite element framework. However, such methods are generally known to suffer from the mesh-density and direction dependence problem as the crack propagation usually occurs along the element edges. This problem was successfully solved via the automatic remeshing [4] or enriching the standard finite element shape functions through a partition of unity method (XFEM) [5], thus making the methods easily

applicable in modelling crack propagation and their use is widespread. Such discrete crack modelling methods are still not without problems as they often lack computational efficiency, especially in three-dimensional computations, or provide spurious damage growth and incorrect solutions when dealing with complex fracture phenomena.

On the other hand, the so-called diffusive crack modeling approaches approximate crack discontinuity by smearing it over the finite volume domain. Such regularization is often controlled by some length-scale parameters. In recent years, a phase-field method which can also be categorized as diffusive crack modeling approach, has gained a great popularity in modelling the crack propagation phenomena. It was developed from the variational approach to fracture [6], thus recasting the original Griffith's fracture theory to the energy minimization problem. It introduces a scalar field (called the phase-field parameter) which can be physically interpreted as the damage variable that continuously varies over the domain between the fully broken and intact material phases. The need to numerically track the displacement field discontinuities is thus averted. In addition, the method is variationally and thermodynamically consistent, and thus no ad hoc criteria are needed to solve the complex fracture processes including the aforementioned crack nucleation, propagation, merging or branching, which significantly simplifies its numerical implementation even in three-dimensional settings, as shown in [7-9]. Nevertheless, it can often be computationally demanding due to the very fine mesh requirement imposed by the aforementioned length-scale parameter. Over the recent years, a great number of studies has been done on the phase-field brittle fracture modeling of homogeneous isotropic media [10-12]. A great overview of the phase-field brittle fracture models is provided in [13].

The phase-field fracture models are more commonly implemented via the robust staggered system approach, because the pure monolithic approaches suffer from the numerical instabilities as a result of the non-convexity of the initial phase-field free energy functional with respect to the phase-field and displacement field [14]. The staggered algorithms uncouple the system of equations to solve it in an incremental-iterative manner [11]. As their efficiency and convergence rate are influenced by the choice of the stopping criterion within the iterative scheme, different stopping criteria have been used, e.g., the normalized change of the system's energy [13] or the successive iteration solution error [9, 14].

The importance of the stopping criterion use was presented in the authors' recent work [15] where the Abaqus [16] implementation of the staggered algorithm with the stopping criterion based on the residual norm control [17] is provided.

In this paper, the use of this algorithm is demonstrated in the heterogeneous microstructure fracture analysis. It should be stressed that the phase-field modelling of the fracture processes occurring at microlevel of heterogeneous materials have been the subject of current research activities in scientific community [18] with many open questions and unresolved issues.

The paper is structured as follows. A brief overview of the phase-field approach to fracture is presented in Section 2. The numerical implementation of the model presented in the authors' former work [15] is outlined in Section 3. The numerical simulations of the fracture process on the simplified microstructural geometry of nodular cast iron are presented in Section 4. Finally, the concluding remarks are drawn in Section 5.

2. Phase-field fracture formulation

Let us consider an elastic n-dimensional body Ω with crack surface $\Gamma(t)$ as presented in Fig. 2.

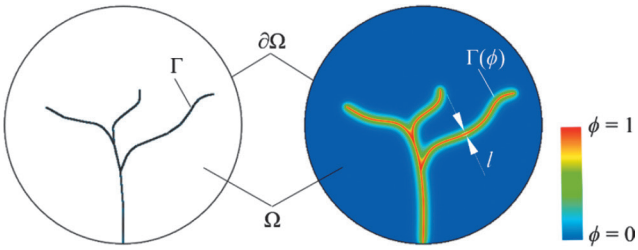

Fig. 2. Elastic n-dimensional body Ω with a discrete (left) and diffusive crack surface (right) [15]

The phase-field fracture approach is then governed by a minimization problem of the free energy functional

$$\Psi = \Psi^{\mathrm{b}} + \Psi^{\mathrm{s}} = \int_{\Omega/\Gamma} \psi_{\mathrm{e}}(\boldsymbol{\varepsilon})\,\mathrm{d}\Omega + \int_{\Gamma} G_{\mathrm{c}}\,\mathrm{d}\Gamma\,, \qquad (1)$$

where Ψ^{b} represents elastic deformation energy, while Ψ^{s} is dissipated fracture surface energy. $\boldsymbol{\varepsilon}$ is small strain tensor, while G_{c} stands for fracture toughness. The dissipated fracture energy corresponds to the creation of new surfaces upon the onset of cracking. It can be seen as an extension of the Griffith's fracture theory [13], where a material fails upon reaching the critical value of the fracture toughness G_{c}. In Eq. (1), ψ_{e} is the elastic strain-energy density function formulated as

$$\psi_{\mathrm{e}} = \tfrac{1}{2}\lambda\,\mathrm{tr}^2(\boldsymbol{\varepsilon}) + \mu\,\mathrm{tr}(\boldsymbol{\varepsilon}^2) \qquad (2)$$

with the Láme constants λ and μ. In the presented regularized framework, the crack geometry is approximated by a smeared representation defined by a scalar *phase-field* parameter $\phi \in [0,1]$, which takes value of 1 for the fully broken material state and the value of 0 for the bulk material (Fig. 2), thus restating the fracture energy Ψ^{s} over the volume domain. Accordingly, the elastic deformation energy part Ψ^{b} is regularized by the introduction of a degradation function $(1-\phi)^2$ to account for the subsequent loss of stiffness in the region representing the diffusive crack (i.e. $\phi \to 1$). The regularized free energy functional can then be written as

$$\Psi(\mathbf{u},\phi) = \int_{\Omega} (1-\phi)^2 \psi_{\mathrm{e}}(\boldsymbol{\varepsilon})\,\mathrm{d}\Omega + \int_{\Omega} \frac{G_{\mathrm{c}}}{2}\left[l(\nabla\phi)^2 + \frac{1}{l}\phi^2 \right]\mathrm{d}\Omega\,, \qquad (3)$$

where l is length scale parameter that regulates the width of the crack band approximation, while $\mathbf{u}$ denotes the displacement field. Furthermore, crack irreversibility is introduced via history field $\mathcal{H}(t) := \max_{\tau=[0,t]} \psi_e(\tau)$ [8] which thus substitutes ψ_e and prevents crack "healing". Governing equations are obtained using the principle of virtual work and can be written as follows

$$\begin{aligned} &\nabla\boldsymbol{\sigma} + \bar{\mathbf{b}} = 0 \quad \text{in } \Omega, \\ &\boldsymbol{\sigma}\cdot\mathbf{n} = \bar{\mathbf{t}} \quad \text{on } \partial\Omega_{\bar{\mathbf{t}}}, \\ &\mathbf{u} = \bar{\mathbf{u}} \quad \text{on } \partial\Omega_{\bar{\mathbf{u}}}, \\ &-G_c l\Delta\phi + \left[\frac{G_c}{l} + 2\psi_e^+\right]\phi = 2\psi_e^+ \quad \text{in } \Omega, \\ &\nabla\phi\cdot\mathbf{n} = 0 \quad \text{on } \partial\Omega, \end{aligned} \tag{4}$$

where $\bar{\mathbf{b}}$ and $\bar{\mathbf{t}}$ are the prescribed volume and surface forces, $\bar{\mathbf{u}}$ is the prescribed displacement, $\mathbf{n}$ is the normal vector on the boundary $\partial\Omega$, and $\boldsymbol{\sigma} = \dfrac{\partial\psi}{\partial\boldsymbol{\mu}}$ is the Cauchy stress. Detailed information on the phase-field fracture formulation can be found in [10].

3. Numerical implementation

The phase-field formulation is implemented into the finite element framework by means of the four-node plane strain element with the standard displacement degrees of freedom and the phase-field parameter ϕ as an additional degree of freedom at each node. The *same shape functions* are applied to interpolate both fields, ϕ and $\mathbf{u}$. Finally, in accordance with the staggered solution scheme, the decoupled system of equations is obtained as follows

$$\begin{aligned} \mathbf{K}^{\phi\phi}\boldsymbol{\phi} &= \mathbf{R}^{\phi}(\mathbf{u},\phi), \\ \mathbf{K}^{\mathbf{uu}}\mathbf{u} &= \mathbf{R}^{\mathbf{u}}(\mathbf{u},\phi), \end{aligned} \tag{5}$$

where $\mathbf{K}^{\mathbf{uu}}$ and $\mathbf{K}^{\phi\phi}$ are stiffness matrices, while $\mathbf{R}^{\mathbf{u}}$ and $\mathbf{R}^{\phi}$ are residual force vectors corresponding to the degrees of freedom $\mathbf{u}$ and ϕ, expressed as

$$\begin{aligned} \mathbf{R}_i^{\mathbf{u}} &= \int_\Omega \mathbf{B}_i^{\mathbf{u}^T}\boldsymbol{\sigma}\,\mathrm{d}\Omega - \int_\Omega \mathbf{N}_i^{\mathbf{u}^T}\bar{\mathbf{b}}\,\mathrm{d}\Omega - \int_{\partial\Omega}\mathbf{N}_i^{\mathbf{u}^T}\bar{\mathbf{t}}\,\mathrm{d}\partial\Omega, \\ \mathbf{R}_i^{\phi} &= \int_\Omega \left\{ G_c l\mathbf{B}_i^{\phi^T}\nabla\phi + \left[\frac{G_c}{l} + 2\mathcal{H}\right]\mathbf{N}_i^{\phi}\phi - 2\mathbf{N}_i^{\phi}\mathcal{H}\right\}\mathrm{d}\Omega, \end{aligned} \tag{6}$$

and

$$\begin{aligned} \frac{\partial\mathbf{R}_i^{u}}{\partial\mathbf{u}_j} &= \mathbf{K}_{ij}^{\mathbf{uu}} = \int_\Omega \mathbf{B}_i^{\mathbf{u}^T}\frac{\partial\boldsymbol{\sigma}}{\partial\boldsymbol{\varepsilon}}\mathbf{B}_j^{\mathbf{u}}\mathrm{d}\Omega, \\ \frac{\partial\mathbf{R}_i^{\phi}}{\partial\boldsymbol{\phi}_j} &= \mathbf{K}_{ij}^{\phi\phi} = \int_\Omega \left\{ G_c l\mathbf{B}_i^{\phi^T}\mathbf{B}_j^{\phi} + \left[\frac{G_c}{l} + 2\mathcal{H}\right]\mathbf{N}_i^{\phi}\mathbf{N}_j^{\phi}\right\}\mathrm{d}\Omega. \end{aligned} \tag{7}$$

In the above equations, $\mathbf{B}$ denotes displacement differentiation matrix, while $\mathbf{N}$ stands for shape function matrix. Fig. 3 shows the flowchart of the staggered algorithm implemented in the FE software Abaqus [16] via the layered user element system generated by UEL and UMAT subroutines. The flowchart corresponds to the updated version of the algorithm [17] which is openly accessible on Mendeley repository. For more information on the updated version, see [17].

Here, the solution estimates ϕ_n^k and $\mathbf{u}_n^k$ are obtained by the Newton-Raphson procedure after the non-converging iteration as follows

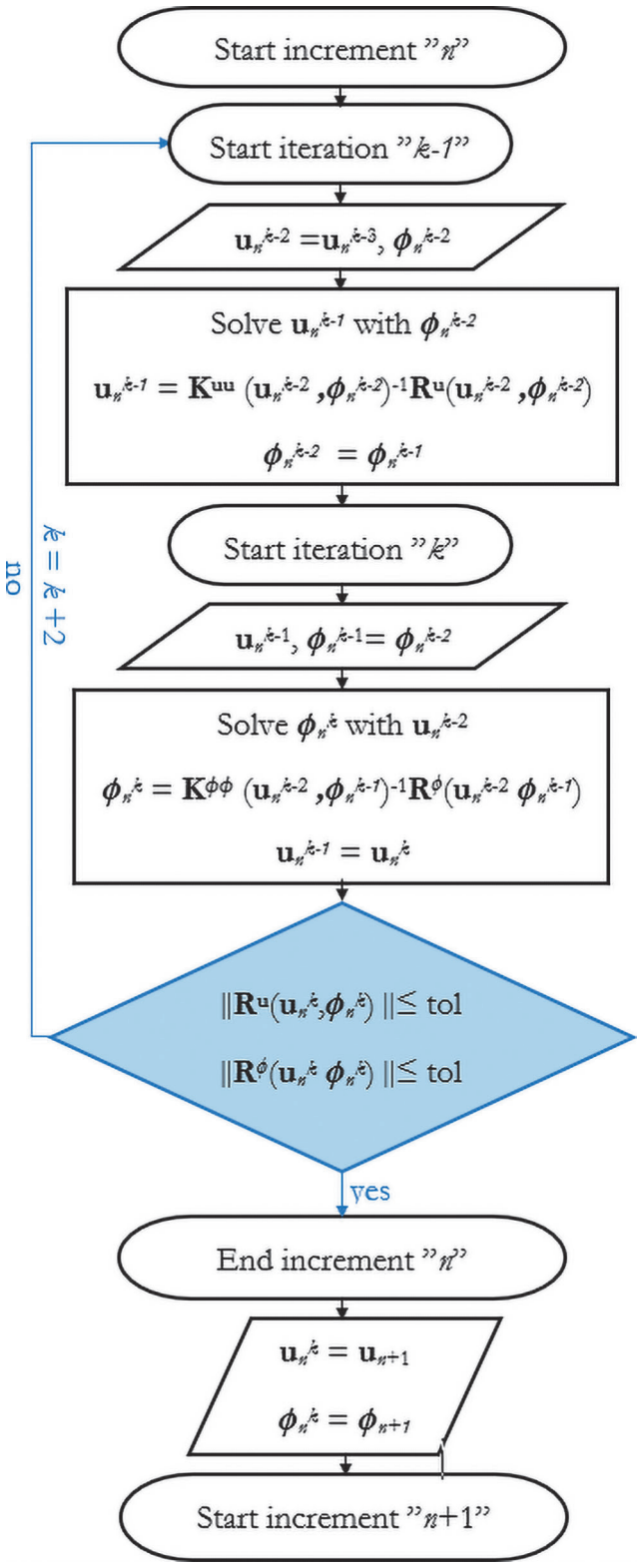

Fig. 3. RCTRL staggered algorithm flowchart [17]

$$\phi_n^k = \phi_n^{k-1} + \mathbf{K}^{\phi\phi}\left(\mathbf{u}_n^{k-2}, \phi_n^{k-1}\right)^{-1} \mathbf{R}^{\phi}\left(\mathbf{u}_n^{k-2}, \phi_n^{k-1}\right),$$
$$\mathbf{u}_n^k = \mathbf{u}_n^{k-1} + \mathbf{K}^{\mathbf{uu}}\left(\mathbf{u}_n^{k-1}, \phi_n^{k-1}\right)^{-1} \mathbf{R}^{\mathbf{u}}\left(\mathbf{u}_n^{k-1}, \phi_n^{k-1}\right). \quad (8)$$

For more details on the numerical implementation, see [15, 20]. The presented phase-field approach has been evaluated and verified on standard benchmark examples in [15] and in the problems of real microstructural geometries in [20], in comparison with the common single iteration staggered algorithm [11]. Here, its capability has been demonstrated through the simulation of the fracture phenomena occurring in the microstructural geometry of the nodular cast iron by the numerical example elaborated in the next section.

4. Numerical examples

The performance of the algorithm is tested on the numerical examples of homogeneous plate subjected to tensile loading and the heterogeneous microstructural geometries.

Homogeneous plate example

A homogeneous 1 × 1 mm plate is discretized by one element as presented in Fig. 4 and subjected to tension. Since the analytical solution is known for this setup, this example is widely used as a test case in the literature, e.g. in [21]. The material properties are chosen as follows: the Young's modulus E = 210 kN/mm^2, Poisson's ratio ν = 0.3 and critical fracture energy density G_c = 2.7 × 10^{-3} kN/mm. The length scale parameter is set to l = 2 mm. The analytical solution

$$\phi = \frac{C\varepsilon_x^2}{\frac{G_c}{l} + C\varepsilon_x^2} \quad (9)$$

is obtained from Eq. (3) setting the crack surface gradient to zero, corresponding to the homogeneous case $(\nabla\phi = 0)$. Thus, the axial stress can be calculated as $\sigma = (1-\phi)^2 C\varepsilon$.

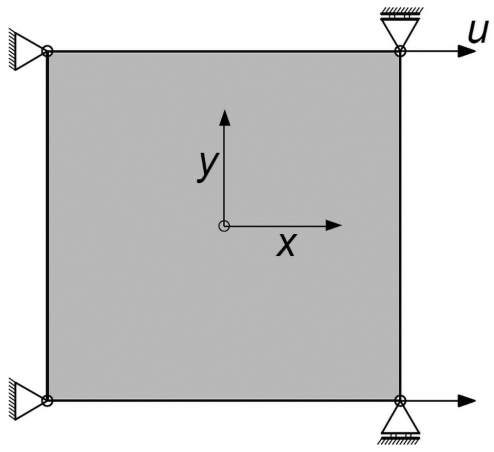

Fig. 4. Geometry and boundary conditions of the homogeneous plate subjected to tension [15]

The example is solved using 4 different loading increments Δu to reach u = 0.01 mm, namely $\Delta u = 2.5\times10^{-3}$ mm, $\Delta u = 5\times10^{-3}$ mm, $\Delta u = 1\times10^{-3}$ mm and $\Delta u = 1\times10^{-4}$ mm. The axial stress-strain response comparison of the residual control staggered algorithm against the analytical solution is presented in Fig. 5. It can be seen that the algorithm matches well with the analytical solution even for large loading increments which is not the case for the staggered algorithms without the iterative loop, as tested in [15].

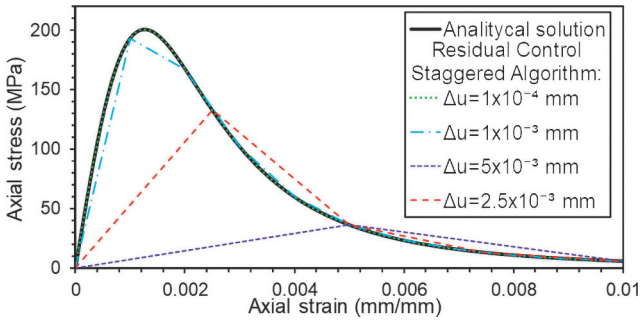

Fig. 5. Stress-strain curves obtained by the residual control staggered algorithm in comparison with the analytical solution.

Heterogeneous microstructure fracture analysis

Fig. 6 shows the heterogeneous microstructure of the nodular cast iron grade EN-GJS-400-18-LT produced by the inmould casting technique and obtained by the metallography in the authors' research team previous work [2, 3]. This ductile nodular cast iron consists of graphite nodules surrounded by a ferritic matrix. For the considered material the volume fraction of graphite nodules is about 7% with circularity of 0.7 (where the value of 1.0 indicates a perfect circle). The academic brittle material properties are used to predict brittle fracture nucleation and propagation because the present algorithm has not been expanded yet to the ductile fracture problem at this moment. As a numerical idealization, the graphite nodules are substituted with spheres. In the considered 2D case, the spheres are projected as circles. Since the academic brittle material properties are already assumed, it seems justified to idealize the nodules as spheres, i.e., circles, to speed up the numerical simulations.

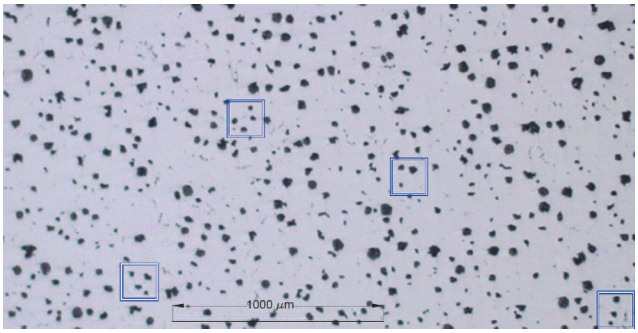

Fig. 6. Metallographic image of EN-GJS-400-18-LT microstructure [3] with the selection of samples satisfying the global average graphite nodules content

Twelve different microstructural samples or Microstructural Volume Elements (MVEs) were randomly selected from the metallographic image while still satisfying the average graphite nodules content of ~7%, as schematically shown in Fig. 6 and Table 1. The size of the samples was 161.7 x 161.7μm. The MVEs were uniformly discretized with ~30 000 finite elements with an average characteristic element length of h = 0.001 mm. The academic material properties are: Young's modulus E = 200 GPa, Poisson's ratio ν = 0.3 and fracture toughness $G_c = 1\times10^3$ N/m. The regularizing parameter was set to l = 0.0025 mm. The displacement boundary conditions imposed on the MVE are presented in Fig. 7.

Table 1. Critical force for different samples under tensile loading

Serial number of MVE	Pore share, %	Critical force, N	Critical force deviation from average, %
1	6.19	282.9	4.16
2	6.53	250.5	7.76
3	5.94	290.0	6.78
4	6.30	282.3	3.94
5	6.74	261.3	3.79
6	6.11	254.4	6.33
7	6.39	281.7	3.72
8	6.21	285.9	5.27
9	6.24	263.9	2.83
10	6.01	276.1	1.66
11	6.30	277.6	2.21
12	6.11	252.5	7.03
Average	6.26	271.6	

The problem was solved with the proposed algorithm in the displacement-controlled regime. Fig. 8 presents crack paths in the simplified geometry of a nodular cast iron microstructure. As evident, the proposed phase-field formulation can successfully calculate the complicated crack paths on the heterogeneous microstructural geometry. The reaction force of the right edge of MVE versus the displacement diagrams for all considered MVEs are shown in Fig. 9.

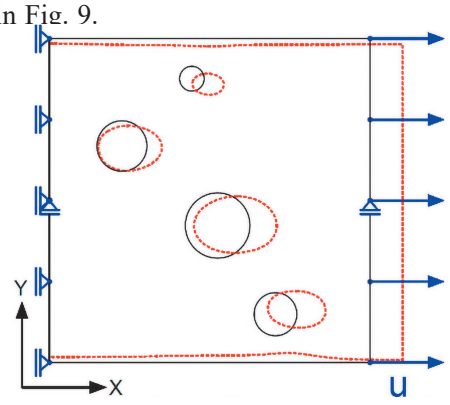

Fig. 7. Displacement boundary conditions imposed on the MVE

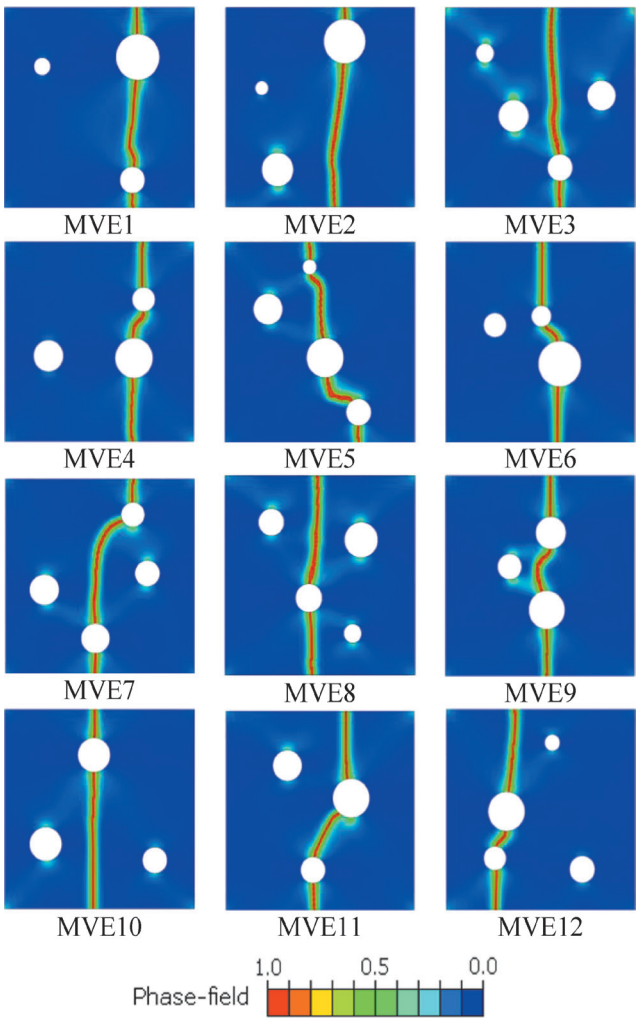

Fig. 8. Crack paths in the simplified geometry of a nodular cast iron microstructure

It is obvious that there is no significant difference in the post-peak behavior of the specimens. In that area the force-displacement curves demonstrate a rapid drop in stiffness after reaching a critical force value as a consequence of an abrupt crack propagation between the microstructural inclusions. Such crack propagation is typical for a class of brittle materials, which is in accordance with the assumptions established in this work. Furthermore, maximum *force and displacement* are shown in Table 1.

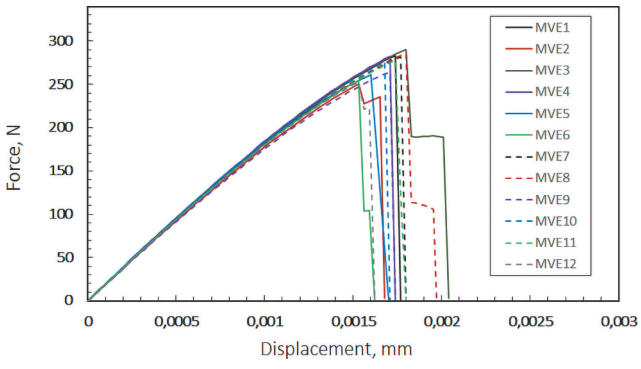

Fig. 9. Force-displacement response for all considered MVEs

5. Conclusions

The fracture analysis of the heterogeneous microstructural geometry based on the microstructural imaging of nodular cast iron was performed for this paper. The phase-field staggered algorithm with residual norm based stopping criterion, recently developed as a part of author's previous study, was utilized. The algorithm was implemented into the finite element program Abaqus by means of the custom linear quadrilateral finite elements with the phase-field parameter as an additional degree of freedom. The concise implementation details are presented together with the verification on the standard benchmark test as well as the demonstration of the model capabilities on the heterogeneous nodular cast iron microstructure represented by the series of MVEs. The obtained results display the ability of the model to capture the brittle crack initiation and propagation, resulting in complex crack paths in heterogeneous microstructural geometries. Although an academic brittle material was employed together with simplifications to geometry, it can still be observed that the maximal deviation of the critical force is not obtained on the MVEs with greatest deviation from average pore share, which shows how the microstructural geometry arrangement also plays a significant role together with porosity ratio. However, it has to be emphasized that the obtained results serve as a demonstration of the algorithms capabilities in complex heterogeneous microstructural geometries and, due to these simplifications, do not represent a realistic material behavior.

References

[1] Hütter, G., Zybell, L., Kuna, M., Micromechanisms of fracture in nodular cast iron: From experimental findings towards modeling strategies – A review. *Eng Fract Mech.*, 144, 118–41 (2015).

[2] Čanžar, P., Tonković, Z., Kodvanj, J., Microstructure influence on fatigue behaviour of nodular cast iron. *Mater Sci Eng A*, 556, 88–99 (2012).

[3] Čanžar, P., Experimental and Numerical Modelling of Fatigue Behaviour of Nodular Cast Iron, Faculty of Mechanical Engineering and Naval Architecture, University of Zagreb, PhD Thesis, 2012 (in Croatian).

[4] Ingraffea, A.R., Saouma, V., Numerical modeling of discrete crack propagation in reinforced and plain concrete. In: Sih G.C., DiTommaso A. (eds) Fracture mechanics of concrete: Structural application and numerical calculation. Engineering Application of Fracture Mechanics, Dordrecht, Springer, 4 (1985).

[5] Moës, N., Dolbow, J., Belytschko, T., A finite element method for crack growth without remeshing. *Int. J. Numer. Methods Eng.*, 46(1), 131–150 (1999).

[6] Francfort, G.A., Marigo, J.J., Revisiting brittle fracture as an energy minimization problem. *Journal of the Mechanics and Physics of Solids*, 46(8), 1319-1342 (1998).

[7] Miehe, C., Aldakheel, F., Raina, A., Phase field modeling of ductile fracture at finite strains: A variational gradient-extended plasticity-damage theory. *International Journal of Plasticity*, 84, 1-32 (2016).

[8] Molnar, G., Gravouil, A., 2D and 3D Abaqus implementation of a robust staggered phase-field solution for modeling brittle fracture. *Finite Elements in Analysis and Design*, 130, 27-38 (2017).

[9] Zhou, S.W., Zhuang, X.Y., Zhu, H.H., Rabczuk, T., Phase field modelling of crack propagation, branching and coalescence in rocks. *Theoretical and Applied Fracture Mechanics*, 96, 174-192 (2018).

[10] Miehe, C., Welschinger, F., Hofacker, M., Thermodynamically consistent phase-field models of fracture: Variational principles and multi-field FE implementations. *International Journal for Numerical Methods in Engineering*, 83(10), 1273-1311 (2010).

[11] Miehe, C., Hofacker, M., Welschinger, F., A phase field model for rate-independent crack propagation: Robust algorithmic implementation based on operator splits. *Computer Methods in Applied Mechanics and Engineering*, 199(45-48), 2765-2778 (2010).

[12] Vignollet, J., May, S., de Borst, R., Verhoosel, C.V., Phase-field models for brittle and cohesive fracture. *Meccanica*, 49(11), 2587-2601 (2014).

[13] Ambati, M., Gerasimov, T., De Lorenzis, L., A review on phase-field models of brittle fracture and a new fast hybrid formulation. *Computational Mechanics*, 55(2), 383-405 (2015).

[14] Bourdin, B., Francfort, G.A., Marigo, J.J., The variational approach to fracture. *Journal of Elasticity*, 91(1-3), 5-148 (2008).

[15] Seleš, K., Lesičar, T., Tonković, Z., Sorić, J., A residual control staggered solution scheme for the phase-field modeling of brittle fracture. *Engineering Fracture Mechanics*, 205, 370-386 (2018).

[16] Abaqus 6.14-1, Dassault Systemes Simulia Corp., Providence, RI, USA, 2014.

[17] Seleš, K., Abaqus Code for a Residual Control Staggered Solution Scheme for the Phase-Field Modeling of Brittle Fracture. https://data.mendeley.com/datasets/p77tsyrbx2/3, Mendeley data (2018).

[18] Nguyen, T.T., Yvonnet, J., Zhu, Q.Z., Bornert, M., Chateau, C., A phase field method to simulate crack nucleation and propagation in strongly heterogeneous materials from direct imaging of their microstructure. *Engineering Fracture Mechanics*, 139, 18-39 (2015).

[19] Bourdin, B., Francfort, G.A., Marigo, J.J., Numerical experiments in revisited brittle fracture. *J. Mechanics and Physics of Solids*, 48(4), 797-826 (2000).

[20] Seleš, K., Jurčević, A., Tonković, Z., Sorić, J., Crack Propagation Prediction in Heterogeneous Microstructure using an Efficient Phase-Field Algorithm. *Theoretical and Applied Fracture Mechanics*, 100, 289-297, (2019).

[21] Molnar, G., Gravouil, A., 2D and 3D Abaqus implementation of a robust staggered phasefield solution for modeling brittle fracture. *Finite Elements in Analysis and Design*, 130, 27-38 (2017).

Tomislav Lesičar[1], Zdenko Tonković[1], Jurica Sorić[1]

Multiscale Modelling of Heterogeneous Structures Using Second-Order Computational Homogenization

[1]Faculty of Mechanical Engineering and Naval Architecture, University of Zagreb, Zagreb, Croatia

Abstract

A second-order two-scale computational homogenization procedure for modelling deformation responses of heterogeneous structures assuming small strains is presented. The macro-to-micro scale transition and generalized periodic boundary conditions on the representative volume element (RVE) are investigated. The macroscale is discretized by means of C^1 two-dimensional triangular finite elements, while standard quadrilateral finite elements are used for the RVE discretization. The new proposed multiscale scheme has been implemented in the finite element software ABAQUS using user subroutine. The efficiency of the proposed multiscale homogenization approach is demonstrated by modelling a pure bending problem.

Keywords: *multiscale analysis, heterogeneous materials, second-order homogenization, C^1 finite element, periodic boundary conditions, Abaqus,*

1. Introduction

In recent years, special attention has been directed to the investigation of mechanical properties of materials and their microstructure since almost all engineering materials can be treated as heterogeneous at some scale of observation. Since classical continuum mechanics does not consider structural effects in the material at microlevels, a large number of multiscale techniques have been developed. In the multiscale procedure, the results obtained by the simulation of RVE, employing some of the homogenization methods, are used for the model at the macrolevel. To solve the microlevel boundary value problem, the finite element (FE) method is mostly used [1,2], but other methods are also available. A more detailed overview of development and application of the multiscale methods is presented in [3,4]. The computational homogenization method does not require an explicit a priori constitutive relation at the macrolevel. This makes its main advantage because it allows modelling complex microstructure geometry, arbitrary non-linear and time dependent material behaviour. Besides the computational homogenization, other homogenization methods are available, mostly developed before the computational homogenization, but in most cases, they are limited to a simple microstructure geometry and small strain constitutive models.

The results obtained by the homogenization, namely the tangent stiffness and the stress tensor depend on the boundary conditions (b. c.) applied on the RVE. Three most commonly used boundary conditions are prescribed displacements, prescribed tractions and periodicity conditions. Homogenization results obtained by prescribed displacements show too stiff homogenized RVE behaviour, while the RVE under traction boundary conditions exhibits too compliant homogenized behaviour. Periodic boundary conditions provide the best homogenization results and the fastest convergence properties by increasing RVE size. As shown in [5], the results obtained by the periodic boundary conditions lie between the values obtained by the prescribed displacements (upper bound) and the prescribed tractions (lower bound). However, periodic b. c. usually require regular RVE discretization on the edges where each node on the independent edge must have a couple node on the dependent edge.

Based on the micro-macro variable dependence, the first-order and second-order homogenization procedures are available. Multiscale analysis using the first-order computational homogenization scheme allows explicit modelling of the microstructure, but retains local concept of the continuum mechanics, and gives satisfactory results only for the simple loading cases. It includes only the first gradient of the macroscopic displacement field and therefore, the size effects cannot be captured. Due to the mentioned shortcomings, the first-order computational homogenization scheme has been extended to the second-order computational homogenization framework, where the second-order stress and strain are included. The formulation is based on a non-local continuum theory which accounts for the influence of an environment on the behaviour of a material point [6,7]. Furthermore, the multiscale analysis using the second-order homogenization approach may describe more complex deformation modes. It requires a more complex formulation at the macrolevel (C^1 continuity), which implicates the requirement that both displacements and deformations must be continuous functions. The microlevel in this case can remain standard keeping micro boundary value problem as simple as possible [8,9]. As well-known, to satisfy C^1 continuity condition, the macrolevel model should be discretized by a higher-order finite element supporting additional degrees of freedom. But finite element formulations suited for nonlocal theory are rather complex and suffer from several drawbacks [10,11]. In addition, some formulations suffer from geometric restraints which may lead to incorrect

results for second-order continuum problems. Therefore, to solve second-order continuum problems, C^0 finite elements based on a mixed formulation have been developed in the last few years, where the displacements and displacement derivatives are considered as independent variables. Their kinematic relation is enforced by Lagrange multipliers [12] or by penalty functions [13].

An important problem in the second-order homogenization framework is the definition of the scale transition methodology for the strains and strain gradients from the macroscale to the discretized microstructure. To establish a relation between the macro and micro variables, due to C^1-C^0 transition, there is a need for an alternative relation between the macrostrain gradient and the microstrain, which results in an additional integral condition of the fluctuation field at the microlevel [9]. There are several approaches to bridge a scale transition with account to the microfluctuation field. In [14], to establish a relation between the macroscopic gradient of the deformation gradient and the microscopic deformation gradient, an auxiliary integral relation has been considered. In integral, the microscopic gradient of the deformation gradient has a definition of a first moment of the deformation gradient. Also, the corner nodes fluctuations are fixed at zero, resulting in artificially stress concentrations. A more consistent approach is used in [15]for example, by Germain, Toupin and Mindlin, and Eringen, gives rise to strain gradient plasticity, and is becoming a common coarse scale basis for multiscale homogenization of material response that respects the non-local nature of heterogeneous fine scale material response. Such homogenization approaches are developed to build either concurrent or hierarchical multiscale computational models for the second gradient response at the coarse scale that represent salient aspects of material response at the fine scale. Typically, the homogenization procedure consists of solving an initial boundary value problem for a statistical volume element of heterogeneous material at the fine scale and computing coarse scale stresses and strains using various volume averaging procedures. By enforcing a kinematically consistent description of the deformation field at each scale and asserting invariance of linear momentum with respect to scale of observation of a fixed set of mass particles, critical features of the boundary conditions and computation of homogenized stresses are revealed. In particular, an internal constraint on the higher-order fluctuation field is required to ensure orthogonality between that part of the fine scale deformation attributed to the second gradient and the part associated with higher-order fluctuations. Additionally, the body forces resulting from such internal constraints must be included in the computation of coarse scale stresses to respect scale invariance of linear momentum at each scale. Numerical implementation of fine scale fluctuation constraints employs linear constraint equations; the computation of coarse scale stresses is facilitated through a multiscale statement of principle of virtual velocities. Example fine scale simulations and associated coarse scale homogenization are presented to illustrate aspects of the boundary conditions using multiple constraint projection matrices. To preserve the classical microstructural boundary value problem, an assumption of the second moment of deformed RVE area was made, resulting in similar integral constraint as in [9]. In [17], the micro displacement field is composed of two components, the local macroscopic displacements and the microfluctuations. The unknown fluctuation field is composed of two unknown functions, related to the first-order and the second-order strain, respectively. However, due to the mathematically rigorous and computationally expensive procedure, this tool is only appropriate for periodic microstructures.

The paper presents the multiscale algorithm using the second-order computational homogenization for a small strain case. Special attention was given to the application of the generalized periodic boundary conditions on the representative volume element (RVE). Besides the generalized periodic boundary conditions, the displacement b. c. were also derived. The macrolevel was discretized by a two-dimensional C^1 triangular finite element, reformulated to the requirements of the second-order computational homogenization from the original formulation for the plate bending problems [18]. The discretization at microlevel was performed using the standard quadrilateral finite elements for plane strain conditions. A computational strategy for the implementation of the imposed integral conditions on the RVE boundary was proposed. All numerical algorithms derived were implemented in FE software ABAQUS [19] using user subroutines. The performance of the proposed formulations is demonstrated by the numerical examples.

The paper is organized as follows. Section 2 briefly discusses the formulation and numerical implementation of the C^1 triangular finite element. In Section 3 the basic relations of a multiscale algorithm with the second-order computational homogenization are derived. The presented multiscale algorithm has been verified on a pure bending problem. Finally, some concluding remarks are given in the last section.

2. 2D C^1 triangular finite element

Strain gradient continuum formulation

The basic strain gradient continuum relations are thoroughly discussed in [9,20]. For two-dimensional problems considered here Latin indices take the values 1 and 2. σ_{ij} and μ_{kij} are the stress tensor and the second-order (double stress) tensor, respectively. An energy conjugate to the stress tensor is the strain tensor represented by $\varepsilon_{ij} = \frac{1}{2}\left(u_{i,j} + u_{j,i}\right)$ with u_i defined as the displacement vector. An energy conjugate to the double stress is a third-order strain gradient tensor $\varepsilon_{ij,k}$. t_i and τ_i are the traction and the double surface traction, respectively. Using the principle of virtual work, ($\delta W_{\mathrm{I}} = \delta W_{\mathrm{E}}$), yields the equilibrium equation

$$\sigma_{ij,j} - \mu_{kij,kj} = 0 \tag{1}$$

Finite element implementation

The relations of nonlocal continuum theory were implemented in the C1 triangular finite element shown in Fig. 1. The element has three nodes, each with twelve degrees of freedom (DOF). The nodal degrees of freedom are the two displacements and their first and second order derivatives with respect to the Cartesian coordinates. The element is called C1PE3, describing C1 continuity and plane strain state. The element displacement field was approximated by the condensed fifth order polynomial. More precisely, 21 coefficients were required for a complete polynomial, but by means of the element degrees of freedom, only 18 equations can be defined. Additional three equations were obtained from the condition that the normal derivative of displacement along the element edge was constrained to vary as a cubic polynomial.

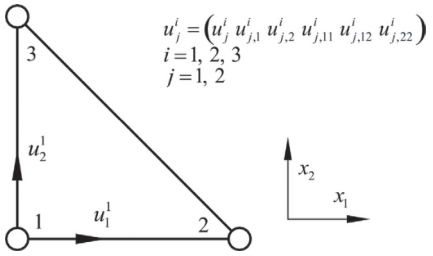

Fig. 1. C^1 triangular finite element

As usually, the element equations are derived from the variation of the principle of virtual work, which may be expressed for strain gradient continuum as

$$\int_A \delta\boldsymbol{\varepsilon}^T \boldsymbol{\sigma}\, \mathrm{d}A + \int_A \delta\boldsymbol{\eta}^T \boldsymbol{\mu}\, \mathrm{d}A = \int_s \delta\mathbf{u}^T \mathbf{t}\, \mathrm{d}s + \int_s \delta\left(\operatorname{grad}\mathbf{u}^T\right)\mathbf{T}\, \mathrm{d}s. \quad (2)$$

In Eq. (2), $_{\sigma}$ and $_{\varepsilon}$ are the stress and strain tensors, respectively. $\boldsymbol{\eta}$ represents the second-order strain tensor containing appropriate second derivatives of the displacement vector $_{\mathbf{u}}$, while $\mathbf{T}$ is the double traction tensor, $\mathbf{T} = \boldsymbol{\tau}\mathbf{n}$. A and s represent area and perimeter of the triangle, respectively. The displacement gradients can be derived as

$$\boldsymbol{\mu} = \begin{bmatrix} \varepsilon_{11} \\ \varepsilon_{22} \\ 2\varepsilon_{12} \end{bmatrix} = \mathbf{B}_{\varepsilon}\, \mathbf{v}, \cdot = \begin{bmatrix} \eta_{111} \\ \eta_{222} \\ \eta_{221} \\ \eta_{122} \\ 2\eta_{121} \\ 2\eta_{212} \end{bmatrix} = \mathbf{B}_{\eta}\, \mathbf{v}, \quad (3)$$

where $\mathbf{B}_{\varepsilon}$ and $\mathbf{B}_{\eta}$ are the matrices containing corresponding the first and second derivatives of the interpolation functions $\mathbf{N}$, and $_{\mathbf{v}}$ represents the vector of nodal degrees of freedom. For nonlinear problems, Eq. (2) was linearized in the time interval (t^{i-1}, t), where t^{i-1} represents the time increment of the last converged equilibrium state, and t is the new affine state obtained in the iterative procedure by updates

$$\begin{aligned} \mathbf{u} &= \mathbf{u}^{i-1} + \Delta\mathbf{u}, \\ \boldsymbol{\sigma} &= \boldsymbol{\sigma}^{i-1} + \Delta\boldsymbol{\sigma}, \\ \boldsymbol{\mu} &= \boldsymbol{\mu}^{i-1} + \Delta\boldsymbol{\mu}. \end{aligned} \quad (4)$$

The increments of the stress $\Delta\boldsymbol{\sigma}$ and the second-order stress $\Delta\boldsymbol{\mu}$ were computed assuming the generalized constitutive relations

$$\begin{aligned} \Delta\boldsymbol{\sigma} &= \mathbf{C}_{\sigma\varepsilon}\Delta\boldsymbol{\varepsilon} + \mathbf{C}_{\sigma\eta}\Delta\boldsymbol{\eta}, \\ \Delta\boldsymbol{\mu} &= \mathbf{C}_{\mu\varepsilon}\Delta\boldsymbol{\varepsilon} + \mathbf{C}_{\mu\eta}\Delta\boldsymbol{\eta}. \end{aligned} \quad (5)$$

In Eq. (5), $\mathbf{C}_{\sigma\xi}$, $\mathbf{C}_{\sigma\eta}$, $\mathbf{C}_{\mu\varepsilon}$ and $\mathbf{C}_{\mu\eta}$ are the material tangent stiffness matrices. By means of standard manipulations in the finite element method, which is also explained in [9] the standard finite element equation was obtained

$$\mathbf{K}\,\Delta\mathbf{v} = \mathbf{F}_{\mathrm{e}} - \mathbf{F}_{\mathrm{i}}. \quad (6)$$

In Eq. (6), stiffness matrix is expressed as

$$\mathbf{K} = \mathbf{K}_{\sigma\varepsilon} + \mathbf{K}_{\sigma\eta} + \mathbf{K}_{\mu\varepsilon} + \mathbf{K}_{\mu\eta}, \quad (7)$$

where the particular submatrices are

$$\begin{aligned} \mathbf{K}_{\sigma\varepsilon} &= \int_A \left(\mathbf{B}_{\varepsilon}^T \mathbf{C}_{\sigma\varepsilon} \mathbf{B}_{\varepsilon}\right)\mathrm{d}A, \quad \mathbf{K}_{\sigma\eta} = \int_A \left(\mathbf{B}_{\varepsilon}^T \mathbf{C}_{\sigma\eta} \mathbf{B}_{\eta}\right)\mathrm{d}A, \\ \mathbf{K}_{\mu\varepsilon} &= \int_A \left(\mathbf{B}_{\eta}^T \mathbf{C}_{\mu\varepsilon} \mathbf{B}_{\varepsilon}\right)\mathrm{d}A, \quad \mathbf{K}_{\mu\eta} = \int_A \left(\mathbf{B}_{\eta}^T \mathbf{C}_{\mu\eta} \mathbf{B}_{\eta}\right)\mathrm{d}A. \end{aligned} \quad (8)$$

Furthermore, $\mathbf{F}_{\mathrm{e}}$ and $\mathbf{F}_{\mathrm{i}}$ are the external and internal nodal force vectors, expressed as

$$\begin{aligned} \mathbf{F}_{\mathrm{e}} &= \int_s \left(\mathbf{N}^T \mathbf{t} + \operatorname{grad}\mathbf{N}^T \mathbf{T}\right)\mathrm{d}s, \\ \mathbf{F}_{\mathrm{i}} &= \int_A \left(\mathbf{B}_{\varepsilon}^T \boldsymbol{\sigma}^{i-1} + \mathbf{B}_{\eta}^T \boldsymbol{\mu}^{i-1}\right)\mathrm{d}A. \end{aligned} \quad (9)$$

The element was implemented in the FE program ABAQUS using the user element subroutine UEL. Using Gauss numerical integration method, stiffness matrix of the C1PE3 element requires 25 points in full integration scheme. To increase numerical efficiency of the multiscale scheme, the reduced integration technique with 13 integration points was used. By reduced integration procedure satisfactory results were provided, without introduction of additional rigid body (zero energy) modes.

3. Scale transition algorithm

The micro-macro algorithm consists of the two models representing two different levels. The first level represents the macromodel. The second level (microstructure) is presented by the representative volume element. In the text that follows the macroscopic quantities are denoted by the subscript "M", while the microscopic values are labelled with the subscript "m". In every macrolevel integration point of the structural mesh, the RVE microanalysis was performed. The macrolevel displacement gradients $\boldsymbol{\varepsilon}_{\mathrm{M}}$ and $\boldsymbol{\eta}_{\mathrm{M}}$ were transformed into the RVE boundary nodal displacements using corresponding boundary conditions. After solving the RVE boundary

value problem, stress $\boldsymbol{\sigma}_M$, double stress $\boldsymbol{\mu}_M$ and constitutive matrices $\mathbf{C}_M$ were obtained by a homogenization procedure. The general scheme of the micro-macro algorithm is presented in Fig. 2 and detailed in [9].

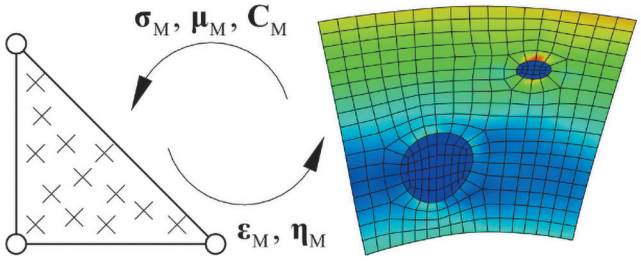

Fig. 2. Scheme of the micro-macro algorithm

In the second-order homogenization the RVE displacement field was obtained by Taylor expansion series as

$$\mathbf{u}_m = \boldsymbol{\varepsilon}_M \mathbf{x} + \frac{1}{2}\mathbf{x}^T \boldsymbol{\eta}_M \mathbf{x} + \mathbf{r} \tag{10}$$

with $\mathbf{x}$ as spatial coordinate on the RVE boundary, and $\mathbf{r}$ representing the microstructural fluctuation field, i.e., the microlevel contribution to the RVE displacement field. The volume average of the microstrain, based on Eq. (10) is expressed as

$$\frac{1}{V}\int_V \boldsymbol{\varepsilon}_m \,\mathrm{d}V = \boldsymbol{\varepsilon}_M + \frac{1}{V}\int_V (\boldsymbol{\eta}_M \mathbf{x})\,\mathrm{d}V + \frac{1}{V}\int_V \operatorname{grad}\mathbf{r}\,\mathrm{d}V, \tag{11}$$

where V represents the RVE volume. To satisfy averaging principles, the second and third terms in the right-hand side of (11) should vanish. By setting the coordinate system origin into the RVE centroid (Fig. 3), the second term was eliminated. The third term must be explicitly imposed

$$\frac{1}{V}\int_V \operatorname{grad}\mathbf{r}\,\mathrm{d}V = \frac{1}{V}\int_A (\mathbf{n}\mathbf{r})\,\mathrm{d}A = \mathbf{0}. \tag{12}$$

The second order strain at the microlevel $\boldsymbol{\eta}_m$ was assumed in the form

$$\boldsymbol{\eta}_m = \int_V \left(\boldsymbol{\varepsilon}_m \mathbf{x} + \mathbf{x}^T \boldsymbol{\varepsilon}_m\right)\mathrm{d}V, \tag{13}$$

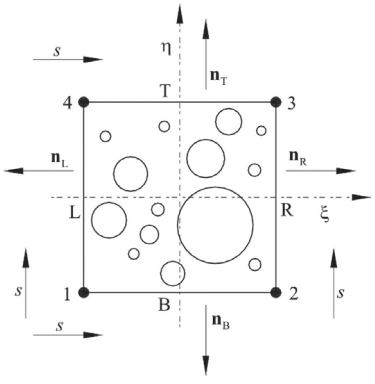

Fig. 3. Representative volume element

according to [9,14]. Inserting of (11) into (13), and after a lengthy procedure gives an additional integral constraint

$$\int_A \left(\mathbf{n}^T \mathbf{r}\,\mathbf{x} + \mathbf{x}^T \mathbf{r}\,\mathbf{n}\right)\mathrm{d}A = \mathbf{0}. \tag{14}$$

The RVE boundary conditions must satisfy constraints (12) and (14). The displacement boundary conditions obey the assumption that $\mathbf{r} = \mathbf{0}$, $\forall \mathbf{x} \in \partial V$, which yields the satisfaction of the two aforementioned relations. The generalized periodic boundary conditions assume identical microfluctuation field on the opposite RVE sides in the form of

$$\begin{aligned} \mathbf{r}_L(s) &= \mathbf{r}_R(s), \\ \mathbf{r}_T(s) &= \mathbf{r}_D(s), \end{aligned} \tag{15}$$

where s is a local coordinate along the edges L, R, T and B standing for the left, right, top and bottom RVE edges. Considering periodicity (15) and to satisfy constraint (14) two additional equations must be prescribed on the independent edges, e.g. left and bottom using Eq. (10), which leads to

$$\begin{aligned} \int_{A_L} \mathbf{u}_L \,\mathrm{d}A &= \boldsymbol{\mu}_M \int_{A_L} \mathbf{x}_L \,\mathrm{d}A + \frac{1}{2}\boldsymbol{\eta}_M \int_{A_L} \left(\mathbf{x}_L^T \mathbf{x}_L\right)\mathrm{d}A, \\ \int_{A_B} \mathbf{u}_B \,\mathrm{d}A &= \boldsymbol{\mu}_M \int_{A_B} \mathbf{x}_B \,\mathrm{d}A + \frac{1}{2}\boldsymbol{\eta}_M \int_{A_B} \left(\mathbf{x}_B^T \mathbf{x}_B\right)\mathrm{d}A. \end{aligned} \tag{16}$$

Homogenization of stress was conducted according to the Hill-Mandel condition

$$\frac{1}{V}\int_V (\boldsymbol{\sigma}_m : \delta\boldsymbol{\varepsilon}_m)\,\mathrm{d}V = \boldsymbol{\sigma}_M : \delta\boldsymbol{\varepsilon}_M + \boldsymbol{\mu}_M \vdots \delta\boldsymbol{\eta}_M. \tag{17}$$

By means of Eq. (17), the homogenized stress tensors can be derived

$$\begin{aligned} \boldsymbol{\sigma}_M &= \frac{1}{V}\int_V \boldsymbol{\sigma}\,\mathrm{d}V = \frac{1}{V}\mathbf{D}\mathbf{f}_b, \\ \boldsymbol{\mu}_M &= \frac{1}{2V}\int_V \left(\boldsymbol{\sigma}_m^T \mathbf{x} + \mathbf{x}^T \boldsymbol{\sigma}_m\right)\mathrm{d}V = \frac{1}{V}\mathbf{H}\mathbf{f}_b. \end{aligned} \tag{18}$$

In Eqs. (18), matrices $\mathbf{D}$ and $\mathbf{H}$ are the coordinate matrices involving all the boundary nodes of the RVE, and $\mathbf{f}_b$ is the vector of boundary RVE nodal forces [9,16]. To obtain homogenized constitutive behaviour as assumed in Eq. (5), the static condensation procedure was employed. By this global RVE stiffness matrix is expressed only by the contributions of the external nodes

$$\tilde{\mathbf{K}}_{bb} = \mathbf{K}_{bb} - \mathbf{K}_{ba}\mathbf{K}_{aa}^{-1}\mathbf{K}_{ab} \tag{19}$$

as described in [9]. $\mathbf{K}_{aa}$, $\mathbf{K}_{ab}$, $\mathbf{K}_{ba}$ and $\mathbf{K}_{bb}$ are the global RVE stiffness submatrices obtained by means of the topological projection matrices, defining internal and boundary contributions. After some straightforward calculus the constitutive operators can be extracted from the RVE in the form of

$$\begin{aligned} \mathbf{C}_{\sigma\varepsilon} &= \frac{1}{V}\mathbf{D}\tilde{\mathbf{K}}_{bb}\mathbf{D}^T, \quad \mathbf{C}_{\sigma\eta} = \frac{1}{V}\mathbf{D}\tilde{\mathbf{K}}_{bb}\mathbf{H}^T, \\ \mathbf{C}_{\mu\varepsilon} &= \frac{1}{V}\mathbf{H}\tilde{\mathbf{K}}_{bb}\mathbf{D}^T, \quad \mathbf{C}_{\mu\eta} = \frac{1}{V}\mathbf{H}\tilde{\mathbf{K}}_{bb}\mathbf{H}^T. \end{aligned} \tag{20}$$

4. Numerical example

A rectangular strip of the length and height of 0.2 m and thickness 1 m subjected to bending was considered. The deformation response of a square model discretized by 16 plane strain triangular finite elements was studied, as shown in Fig. 4. The imposed loading and boundary conditions reproduced the deformed configuration of the macro model displaying constant curvature. The material considered was an academic example of a steel with porous microstructure. The material data were the Young's modulus E = 210 GPa, the Poisson's ratio v = 0.3, the yield stress of 250 MPa and the elastoplastic tangent modulus of 250 MPa describing isotropic hardening. Two RVEs with the porosities of 13% and 27% randomly distributed voids were analysed, as presented in Fig. 5. The side length of the RVEs is taken 0.2 mm. For the sake of comparison, the homogeneous structure was also considered. The microlevel discretization with 13% voids of the average radius of 0.043 mm was performed by 508 quadrilateral finite elements, while the discretization of the RVE with 27% voids of the average radius of 0.0086 mm was carried out using 1198 quadrilateral elements.

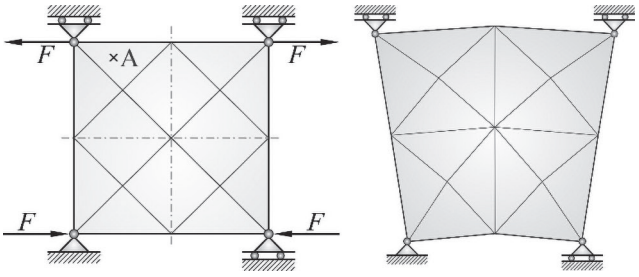

a) b)

Fig. 4. Pure bending problem: a) discretization and loading, b) deformed configuration

The moment-curvature diagram presenting the deformation responses for the two different computational variants is shown in Fig. 6. The diagram displays that the stiffness of the analysed specimens significantly decreased when the material porosity increased from 13% to 27 %, as expected. Accordingly, for the same curvature the bending moment was significantly reduced if porosity increased. It should be stressed that the computational results display the realistic structural behaviour,

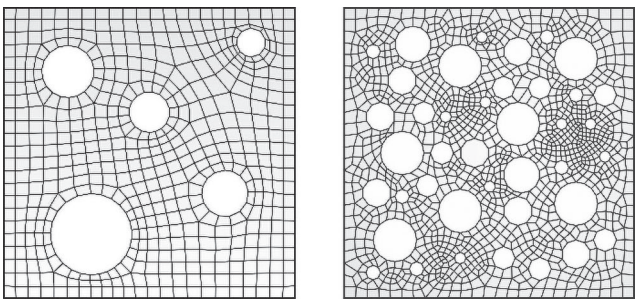

a) b)

Fig. 5. Representative volume elements with a) 13% voids, b) 27% voids

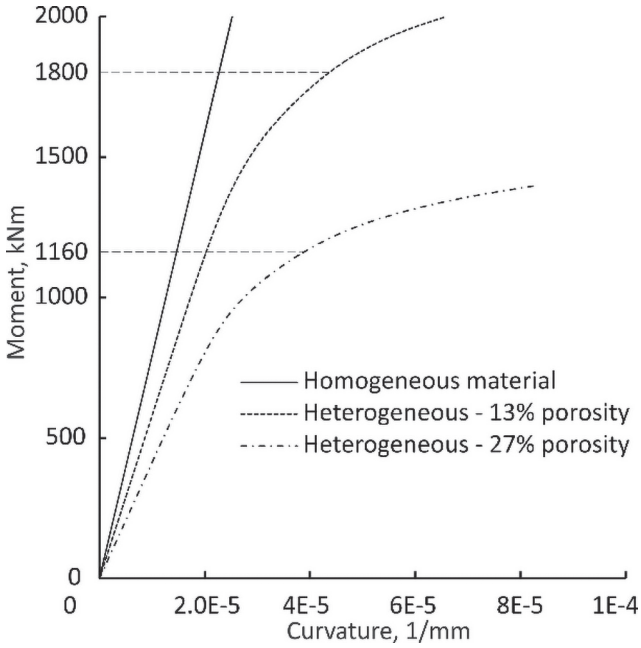

Fig. 6. Moment-curvature diagram

which demonstrates the accuracy of the proposed computational algorithms.

The distribution of the effective plastic strain over the deformed RVEs at the integration point A shown in Fig. 4, for the two different bending moments, which are associated to different curvatures, for the porosities displayed in Fig. 5 are presented in Figs. 7 and 8.

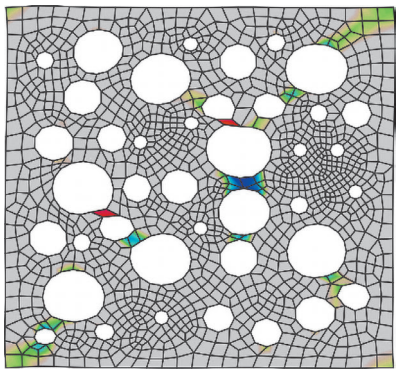

Fig. 7. Distribution of effective plastic strain over RVE at integration point A for bending moment of 1160 kNm and porosity of 27%

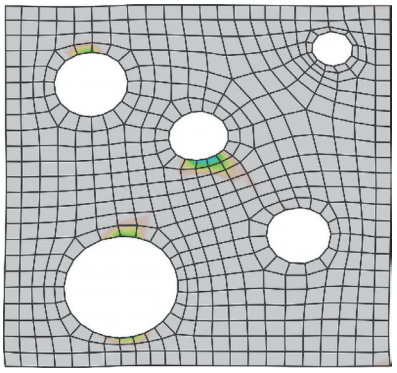

Fig. 8. Distribution of effective plastic strain over RVE at integration point A for bending moment of 1800 kNm and porosity of 13%

It is obvious in Fig. 6 that the structure consisting of the material with the 13% of porosity remains in the elastic range at the bending moment of 1160 kNm, while a nonlinear response is displayed in the case of 27% voids. For the larger porosity Fig. 7 shows that the microstructural shear bands between voids are developed in. At the bending moment of 1800 kNm, the plastic zones occur only in the small local domains around the voids in the material with 13% porosity. It can be observed that the deformed RVEs were not able to demonstrate the macroscopic deformation pattern because of very large ratio between the microscopic and macroscopic side lengths. The microscopic curvature would be more pronounced, if a larger RVE size had been used. It is known that the determination of the RVE represents an important issue in the homogenization concept. This is particularly important in the second-order homogenization approach, where the nonlocal influence is in direct correlation to the RVE size. However, the RVE determination and its influence on the structural responses is beyond the scope of this paper.

5. Conclusions

A micro-macro computational strategy employing the second-order computational homogenization scheme for heterogeneous materials at small strains has been presented. According to the second-order formulation, the macrolevel was discretized by the C1 plane strain triangular finite element based on the strain gradient theory, while the standard C0 quadrilateral finite element was used for the discretization at the microlevel. The C1 element derived for nonlinear analysis was implemented in the FE software ABAQUS by means of the user-defined subroutine UEL. In the frame of the second-order computational homogenization, issues related to the application of the boundary conditions on the representative volume element at the microlevel were discussed. Herein, both the displacement and the generalized periodic boundary conditions are considered. The new proposed multiscale computational strategy has been again implemented in the ABAQUS via user subroutines UEL at the macrolevel, and via UELMAT at the microlevel. In order to impose the microfluctuation constraint, it was demonstrated in [9] that trapezoidal rule gives a physically correct deformation response.

Efficiency and accuracy of the proposed multiscale approach is demonstrated by a typical numerical example in multiscale analysis, the pure bending problem. The realistic deformation responses of the models at both scales demonstrate the accuracy of the proposed computational approach.

References

[1] Brekelmans, W.A.M., Geers, M.G.D., Kouznetsova, V.G., Computational Homogenisation for Non-Linear Heterogeneous Solids. In: *Multiscale Modeling in Solid Mechanics*, 1–42 (2009).

[2] Nguyen, V.D., Becker, G., Noels, L., Multiscale computational homogenization methods with a gradient enhanced scheme based on the discontinuous Galerkin formulation. *Comput Methods Appl Mech Eng*., 260, 63–77 (2013).

[3] Matouš, K., Geers, M.G.D., Kouznetsova, V.G., Gillman, A., A review of predictive nonlinear theories for multiscale modeling of heterogeneous materials. *Mechanics of Materials*, 330, 192–220 (2017).

[4] Geers, M.G.D., Kouznetsova, V.G., Brekelmans, W.A.M., Multi-scale computational homogenization: Trends and challenges, *J Comput Appl Math*., 234(7), 2175–2182 (2010).

[5] Miehe, C., Koch, A., Computational micro-to-macro transitions of discretized microstructures undergoing small strains. *Arch Appl Mech*., 72(4–5), 300–317 (2002).

[6] Mindlin, R.D., Second gradient of strain and surface-tension in linear elasticity. *Int J Solids Struct*., 1(4), 417–438 (1965).

[7] Toupin, R.A., Theories of elasticity with couple-stress. *Arch Ration Mech Anal*., 17(2), 85–112 (1964).

[8] [8] Kouznetsova, V.G., Geers, M.G.D., Brekelmans, W.A.M., Multi-scale second-order computational homogenization of multi-phase materials: a nested finite element solution strategy, *Comput Methods Appl Mech Eng*., 193, 5525–50 (2004).

[9] Lesičar, T., Tonković, Z., Sorić, J., A second-order two-scale homogenization procedure using C1 macrolevel discretization. *Comput Mech*., 54(2), 425–441 (2014).

[10] Petera, J., Pittman, J.F.T., Isoparametric Hermite elements. *Int J Numer Methods Eng*., 37(20), 3489–3519 (1994).

[11] Zervos, A., Papanastasiou, P., Vardoulakis, I., Modelling of localisation and scale effect in thick-walled cylinders with gradient elastoplasticity. *Int J Solids Struct*., 38(30–31), 5081–95 (2001).

[12] Amanatidou, E., Aravas, N., Mixed finite element formulations of strain-gradient elasticity problems. *Comput Methods Appl Mech Eng*., 191, (1723–51) (2002).

[13] Zervos, A., Papanicolopulos, S., Vardoulakis, I., Two Finite-Element Discretizations for Gradient Elasticity. *J Eng Mech*., 135(3), 203–13 (2009).

[14] Kouznetsova, V.G., Geers, M., Brekelmans, W.A.M., Size of a Representative Volume Element in a Second-Order Computational Homogenization Framework. *Int J Multiscale Comput Eng*., 2(4), 24 (2004).

[15] Luscher, D., McDowell, D., Bronkhorst, C., Essential Features of Fine Scale Boundary Conditions for Second Gradient Multiscale Homogenizaton of Statistical Volume Elements. 10(5), 461–86 (2012).

[16] Kaczmarczyk, L.K., Pearce, C.J., Bicanic, N., Scale transition and enforcement of RVE boundary conditions in second-order computational homogenization. *Int J Numer Methods Eng*., 74(3), 506–22, 2008.

[17] Bacigalupo, A., Gambarotta, L., Second-order computational homogenization of heterogeneous materials with periodic microstructure. *ZAMM - J Appl Math Mech / Zeitschrift für Angew Math und Mech*., 90(10–11), 796–811, (2010).

[18] Dasgupta, S., Sengupta, D., A higher-order triangular plate bending element revisited. *Int J Numer Methods Eng*., 30(3), 419–30 (1990).

[19] Abaqus 6.14-1, Dassault Systemes Simulia Corp., Providence, RI, USA, 2014.

[20] Lesičar, T., Tonković, Z., Sorić, J., Two-scale computational approach using strain gradient theory at microlevel. *Int J Mech Sci*., 126, 67-78 (2017).

Mato Perić[1], Ivica Garašić[2], Zdenko Tonković[2]

Numerical Modelling and Experimental Investigation of the Buried Arc Welding Process

[1]Bestprojekt, Bureau of Energetics and Mechanical Engineering Ltd., Zagreb, Croatia
[2]Faculty of Mechanical Engineering and Naval Architecture, University of Zagreb, Zagreb, Croatia

Abstract

This paper presents a numerical and experimental study of residual stresses induced by the buried arc welding process in a butt-welded plate sample. Within the framework of numerical investigations, a thermo-mechanical finite element analysis was performed by applying the element birth and death technique in the thermal analysis, while the mechanical analysis was performed simultaneously in one step to reduce simulation time. To validate the numerical model, a series of experiments using a fully automated welding process were conducted. Temperature and residual stress measurements were performed by using thermocouples and hole-drilling stress relaxation method. Furthermore, the heat input efficiency for the buried arc welding process was determined by using a parametric analysis.

Keywords: *buried arc welding, butt-welded plates, residual stress, modified MAG welding, thermocouples, hole-drilling method.*

1. Introduction

Butt joint and T-joint welded plates are frequently used in shipbuilding, offshore, power plants, civil engineering and many other industrial fields as fundamental members of various structures. In engineering practice, the welding of such structures is commonly performed by Metal Active Gas (MAG) welding technique that is accompanied by a large heat input, which leads to local melting of the material through the addition of a molten metal electrode. An inevitable and harmful consequence of this process is that due to the rapid cooling in the material, residual stresses and permanent deformations occur with microstructural changes in the welded joint. In the presence of cracks in the material, tensile residual stresses in combination with workload accelerate their growth and lead to shorter life of structures [1].

The main disadvantages of such conventional MAG welding procedure are visible in the welding of thick plates where a huge number of weld passes are needed that significantly increases production time [2]. A reasonable solution to the high-productive welding of thick plates could be in a modified MAG welding process that utilizes the specific high penetration arc phenomena i.e. buried arc. This type of arc has been known from earlier but is very rarely used in MAG welding due to its arc instability. In recent years, due to its technical progress, buried arc welding has become a very attractive tool in the welding of thick plates.

Since there is still no adequate data available in the literature for this specific arc mode transfer, the goal of this study is to investigate the thermal and residual stress fields caused by buried arc welding numerically and experimentally. Consequently, it is of great interest to analyse the weld joint characteristics as well as thermal history and distortions due to the relatively high heat input and specific heat distribution in the weld pool area.

During the *last decades*, finite element (*FE*) *simulations* of welding processes *have become* important tools for **predicting welding** residual stresses and distortions. In principle, this simulation consists of two main parts: thermal analysis and mechanical stress analysis [3–7]. In thermal analysis, the temperature field is determined as a function of time for each integration point. This temperature time-history is used as an input into thermal stress analysis. Herein, the thermal solution can be sequentially or fully coupled with the mechanical solution of the structure. Because the rate of heat generation due to mechanical dissipation energy can be neglected in heat transfer analysis, sequentially coupled thermal-stress analysis is commonly applied for the simulation of the welding process in which thermal analysis is followed by stress analysis [8–11].

In this study, welding experiments were conducted using the fully automated buried arc welding process. Here, the temperature and residual stress measurements were performed by using thermocouples and hole-drilling stress relaxation method and the test results were compared with those obtained from the finite element analyses. The paper is organized as follows. Section 2 contains a description of the buried arc welding procedure. In Section 3, the experimental set-up is provided where the welding conditions, thermal and residual stress measurements are discussed in detail. Next, in Section 4, a numerical model is presented. Section 5 contains comparisons of the experimentally measured and numerically calculated temperature histories and residual stresses induced by the buried arc welding of two steel plates. Finally, some concluding remarks are given in the last section.

2. Description of buried arc welding process

Enhanced welding productivity is one of the main goals to be achieved and it is projected through two aspects; larger metal deposit and deeper penetration. This is possible to obtain through increase of current and consequently voltage in the electric arc. However, beyond spray arc area severe rotation of the arc is present that is very difficult to control. From this aspect, MAG technology offers a variety of so-called modified processes which enable metal transfer and improved operational stability in parameter area where conventional processes are unstable or result in some irregularities like spattering or lack of fusion. Such modified processes could be achieved in low and high end of MAG parameter area, that is to say, at low and high currents. While low currents are suitable for thin plates and root welding, high currents are applied in thick plates welding. The buried arc MAG welding is suitable for application in thick plate welding. The definition of the buried arc emphasizes that due to decreases of the arc voltage, the arc is generated and positioned below the melted metal surface and high currents are simultaneously applied in order to achieve better penetration and higher welding deposits (Fig. 1) [12].

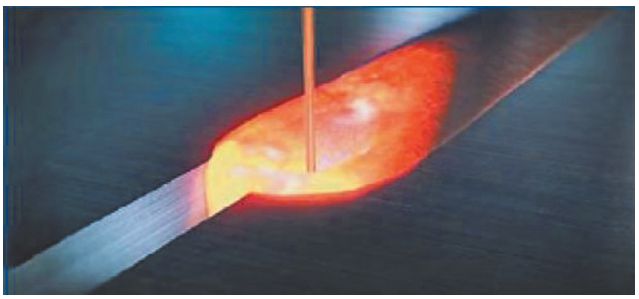

Fig. 1. Buried arc process [13]

In comparison to the conventional arc interaction, the heat input by the buried arc is applied to a deeper portion of the plate, and thus very deep penetration can be obtained. Furthermore, comparing to a conventional MAG process which is generally carried out using currents below 500 A, the buried arc utilizes higher currents. Development of equipment that utilizes waveform control where arc continuously pressurizes the side portion of the molten metal using an appropriate current-voltage cycle enables the stable application of the buried arc.

From an economic aspect buried arc application is superior to conventional MAG welding. Due to better penetration, the preparation of welding bevels is applied with smaller opening angles. The number of passes can be reduced as well as the complete welding time and the amount of distortions. The consumption of wire and gas is also smaller, thus a general cost reduction could be achieved. On the other hand, because of high current applications and large deposits, only robotic and automatic means are utilized to perform the process. However, due to high industrial demands the manual process is also being developed. A water-cooled torch is required as well as a robust system for wire feeding as wire speed can achieve up to 60 m/min, depending on the diameter. A detailed comparison between conventional MAG welding and buried arc welding is recently presented in the authors' earlier work [14].

3. Experimental measurements

The geometry of two plates welded into a butt joint, including the relevant dimensions, is presented in Fig. 2. The welding was performed by the buried arc welding procedure using a 7-axis robot system (Fig. 3) supplied by a two parallel 500 A digital inverter power source to ensure sufficient current and to obtain buried arc at high current level. The plates are made of low-carbon steel EN 10025-2: S355J2+N for which the thermal and mechanical properties depending on the temperature and chemical composition are adopted from [14]. A joint preparation with a 3 mm gap and ceramic backing is applied in order to achieve complete penetration and secure molten metal. A *water circulation system* was applied for the closed loop *cooling of the torch.* The weld-

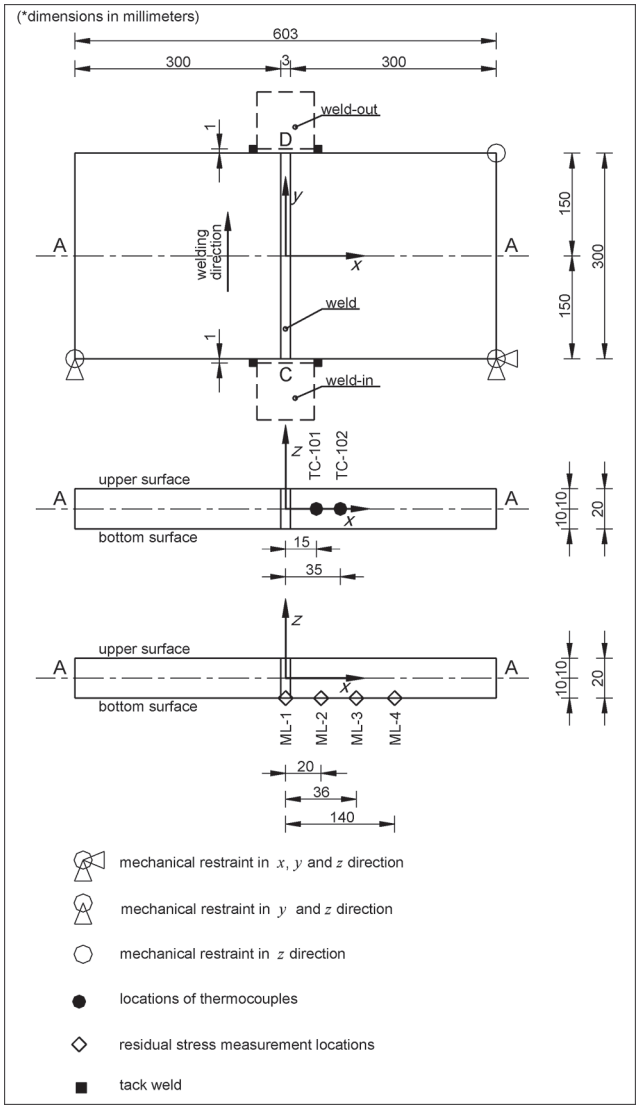

Fig. 2. Geometry of two butt-welded plates

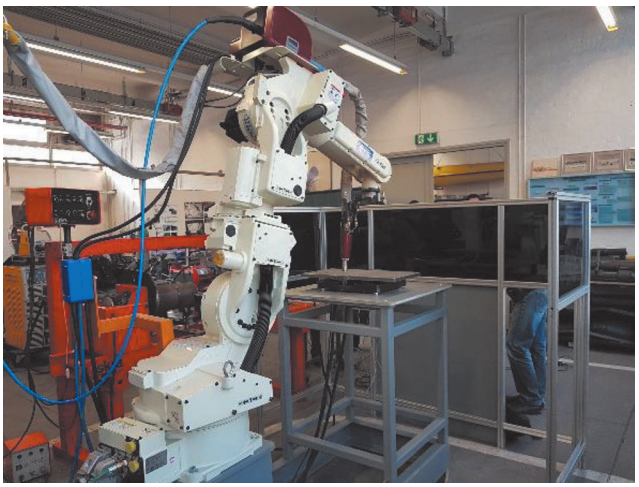

Fig. 3. Experimental setup of two butt-welded plates

ing parameters chosen for this procedure were as follows: wire diameter 1.6 mm, composition of shielding gas 100% CO_2, gas flow 25 l/min, wire feed speed 12.3 m/min, welding current I = 540 A, welding voltage U = 41 V and welding speed v = 300 mm/min. The welding procedure was completed in a single pass with neutral welding gun inclination.

The temperature measurements during the welding process and cooling time were conducted using two thermocouples (Type K). They were denoted as TC-101 and TC-102 and located in the middle plane of the welded sample, as shown in Fig. 2.

For the residual stress measurements, another butt-welded sample was made to completely eliminate the influence of the thermocouple holes in the residual stress state. The measurement of residual stresses was performed by applying the hole-drilling strain-gauge method of stress relaxation using the Vishay RS200 device (Figure 4). The measurement locations of four strain gauges for determination of residual stress are shown in Figure 2.

Fig. 4. Measurement of residual stresses

4. Numerical model

As mentioned in the Introduction section, the welding simulation process consists of two independent analyses, i.e. thermal and mechanical ones. In the thermal analysis, the welding process was performed by applying a uniformly distributed heat flux per weld volume, $Q = \eta UI/V_H$, where η represents the efficiency of the heat input and V_H is heat source volume. The heat flux input applied to the weld was $Q = 6.27 \times 10^{10}$ $Jm^{-3}s^{-1}$. Furthermore, the following data are assumed: convection heat transfer coefficient h_c = 10 $Wm^{-2}K^{-1}$ and surface emissivity ε = 0.9. In the here presented study, the heat input efficiency for the buried arc welding process was determined using parametric analysis and by varying parameter η until a good match between the numerically predicted temperatures and experimental measurements was achieved [15]. It is concluded that the best results are obtained when η = 85%, thus this value is taken in the numerical calculations. A similar investigation of welding process efficiency based on the comparison of numerically and experimentally obtained data was performed by Kollár et al [16].

During thermal analysis, the element birth and death method was applied to simulate weld filler deposition. The obtained temperature-dependent thermal field was then used as an input load in mechanical analysis. To accelerate the simulation process, a simultaneous weld deposition [17-19] was applied in mechanical analysis. In thermal analysis, DC3D8 three-dimensional eight-node brick finite elements were used, while C3D8I elements with incompatible modes were used in mechanical analysis. Here, an elastic-perfectly plastic behaviour material model was assumed. The mechanical boundary conditions are given in Fig. 2.

The same finite element mesh consisting of 36,960 finite elements (Fig. 5) was used in both thermal and mechanical analysis. A very fine mesh of finite elements was used in the weld bead and its vicinity, while the area far away from the weld was discretised with a coarser mesh to reduce the overall model size. The mesh sensitivity analysis was presented in the authors' previous study [14]. In the FE model it is assumed that the base metal and weld metal have the same thermal and mechanical properties and the creep strains were not taken into account. Moreover, the influence of the phase transformations on the residual stress and deformation state was neglected, as it is insignificant in low-carbon steel [5]. All the computations were performed within the FE software Abaqus/Standard [20].

5. Results and discussion

5.1. Thermal analysis

The numerically and experimentally obtained temperature-time histories for the first 700 s after the start of welding at the two thermocouple locations TC-101 and TC-102 are given in Fig. 6. As the numerically calculated temperatures are almost identical to the experimentally measured ones, it can be concluded that the implemented thermal material properties are very close to the real ones. The full field cooling processes for 173 and 381 s after the start of welding are given in Figs. 7a and 7b.

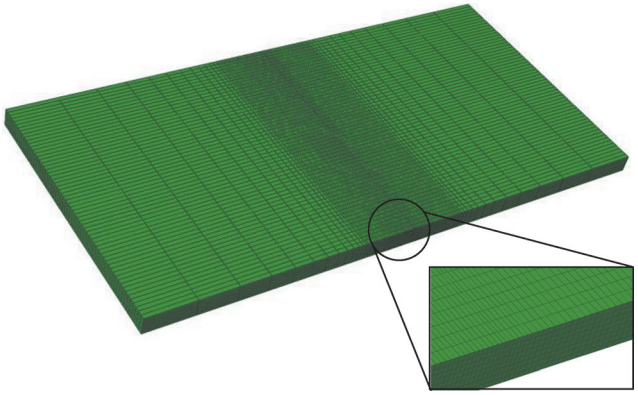

Fig. 5. Finite element mesh of two butt-welded plates

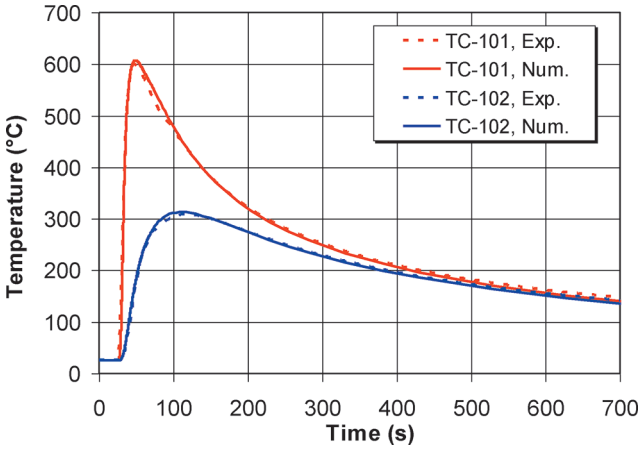

Fig. 6. Temperature-time histories at nodes TC-101 and TC-102

5.2. Mechanical analysis

The residual stresses in the weld direction along the line A-A, seen in Fig. 2, on the lower surface of the plate are presented in Fig. 8. By comparing the numerical and experimental results, it is apparent that their trend is very similar. As seen in Fig. 8, the tensile stresses at the weld line reach the yield strength of the material, which then decreases to zero, finally becoming compressive at distances far from the weld line. The calculated tensile transversal stress peaks near the weld are 237 MPa (Fig. 9) and vanish at the end of the plates. In Fig. 9 it can be seen that the measured transversal stress approximately follows the numerically calculated one. The difference between the measured and calculated residual stresses can be attributed to the introduced initial stresses during steel production. A feasible procedure to eliminate initial stresses is to anneal the plates at high temperatures. Unfortunately, the annealing procedure before the start of welding was not performed in this study.

The full field longitudinal and transversal residual stress distributions are given in Figs. 10a and 10b.

6. Conclusions

In the frame of this study a numerical model for the simulation of thick steel plate butt-welding using high-productive buried arc technology was proposed and

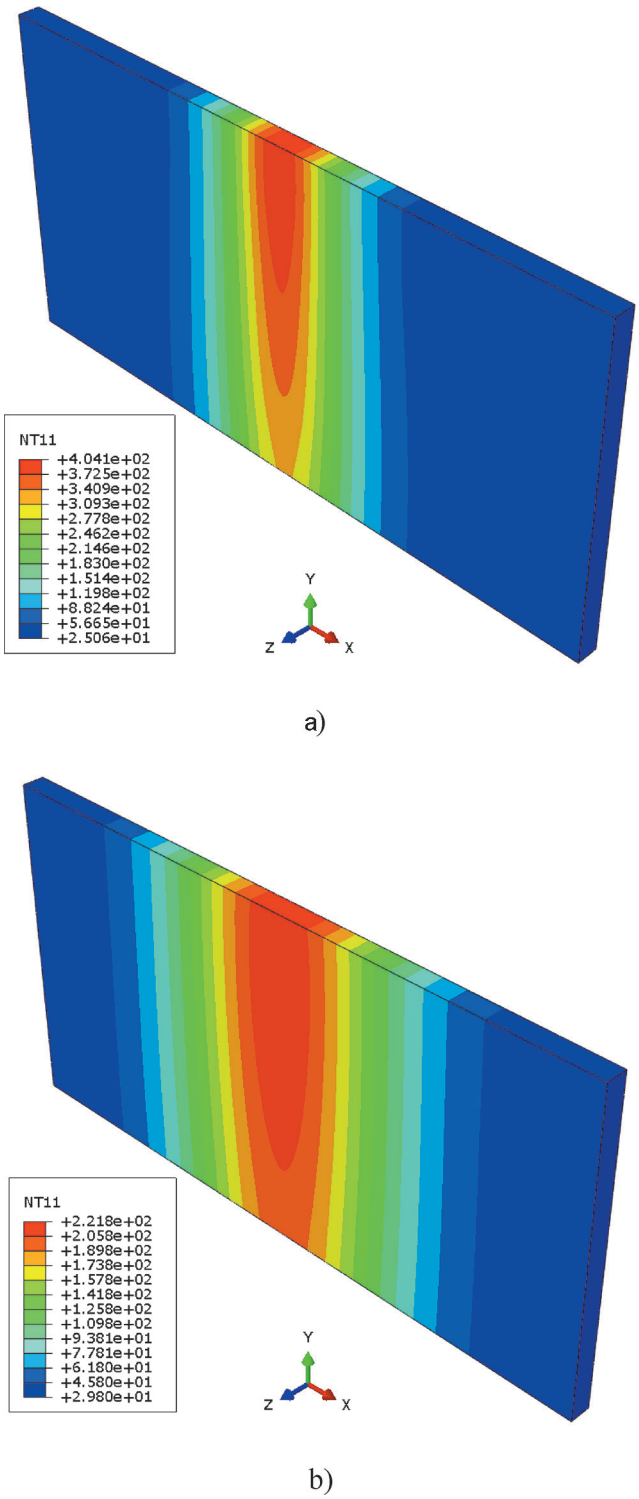

Fig. 7. Full field temperature distributions: a) 173 s after welding start, b) 381 s after welding start

experimentally validated. In the thermal part of the numerical analysis the element birth and death method was used for the numerical simulation of filler metal deposition, while a simplified heat flux with uniformly distributed heat flux per weld volume was employed.

The mechanical part of the numerical analysis was done simultaneously in one step to speed up the calculation process. The main conclusions can be summarized as follows:

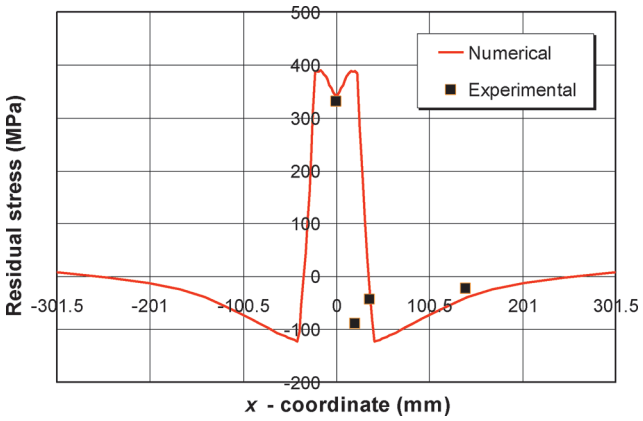

Fig. 8. Residual stresses in the weld direction along the line A–A shown in **Fig. 2,** on the lower surface of the plate in comparison with experimental measurements

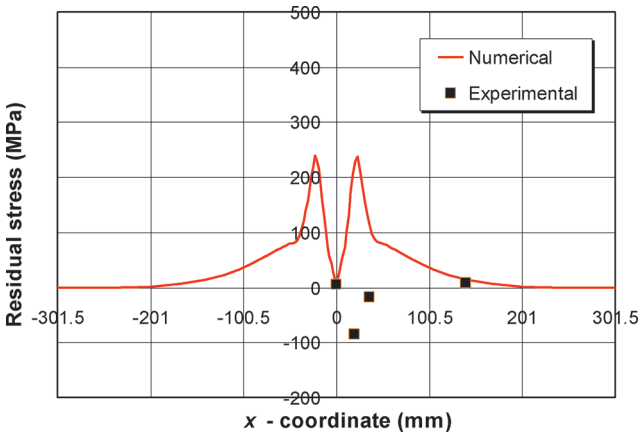

Fig. 9. Transversal residual stresses along the line A–A shown in **Fig. 2,** on the lower surface of the plate in comparison with experimental measurements

- The numerically calculated and experimentally measured temperature histories agree very well. The estimated differences are under 1.5%.
- The heat input efficiency for the buried arc welding process was determined using parametric analysis and its value was found to be around 85%.
- The numerically calculated and experimentally obtained longitudinal stresses were tensile in the weld and its vicinity.
- The numerically calculated transversal stresses tended to be about zero in the weld and its vicinity, otherwise they were tensile.

Based on the experimental measurements regarding temperature and residual stress fields, it can be pointed out that the suggested numerical model is suitable for the numerical simulation of buried arc welding.

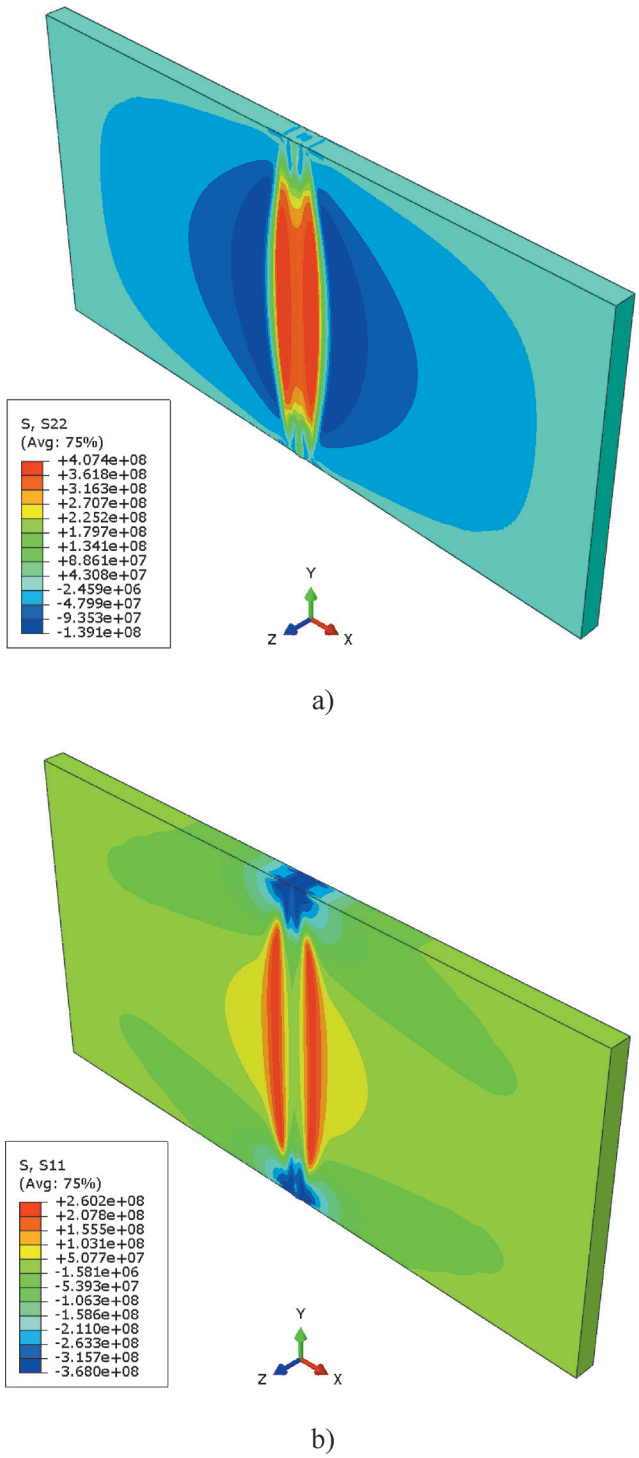

Fig. 10. Full field residual stress distributions: a) longitudinal and b) transversal directions, (N/m^2)

References

[1] Chen, Z., Xiong, Y., Qiu, H., Lin, G., Li, Z., Stress intensity factor-based prediction of solidification crack growth during welding of high strength steel. *J Mater Process Technol*, 252, 270–278 (2018).

[2] Pu, X., Zhang, C., Li, S., Deng, D., Simulating welding residual stress and deformation in a multi-pass butt-welded joint considering balance between computing time and prediction accuracy. *Int J Adv Manuf Technol*, 93(5-8), 2215–2226 (2017).

[3] Deng, D., Liang, W., Murakawa, H., Determination of welding deformation in filletwelded joint by means of numerical simulation and comparison with experimental measurements. *J Mater Process Technol*, 183, 219–225 (2007).

[4] Lee, C.H., Chang, K.H., Three-dimensional finite element simulation of residual stresses in circumferential welds of

steel pipe diameter effects. *Mater Sci Eng A*, 487, 210–218 (2008).

[5] [5] Deng, D., FEM prediction of welding residual stress and distortion in carbon steel considering phase transformation effects. *Mater Des*, 30, 359–366 (2009).

[6] [6] Gannon, L., Liu, Y., Pegg, N., Smith, M., Effect of welding sequence on residual stress and distortion in flat-bar stiffened plates. *Mar Struct*, 23, 385–404 (2010).

[7] [7] Long, H., Gery, D., Carlier, A., Maropoulos P.G., Prediction of welding distortion in butt joint of thin plates. *Mater Des*, 30, 4126–35 (2009).

[8] [8] Barsoum, Z., Lundback, A., Simplified FE welding simulation of fillet welds – 3D effects on formation residual stresses. *Eng Fail Anal*, 16, 2281–2289 (2009).

[9] [9] Teng, T.L., Fung, C.P., Chang, P.H., Yang, W.C., Analysis of residual stresses and distortions in T-Joint fillet welds. *Int J Press Vess Pip*, 78, 523–538 (2001).

[10] [10] Shan, X., Davies, C.M., Wangsdan, T., O'Dowd, N.P., Nikbin, K.M., Thermo-mechanical odelling of a single-bead-on-plate weld using finite element method. *Int J Press Vess Pip*, 86, 110–21 (2009).

[11] [11] Wang, R., Zhang, J., Serizawa, H., Murakawa, H., Study of welding inherent deformations in thin plates on finite element analysis using interactive substructure method. *Mater Des*, 30, 3474–3481 (2009).

[12] [12] Baba, H., Era, T., Ueyama, T., Tanaka, M., Single pass full penetration joining for heavy plate steel using high current GMA process. *Weld World*, 61(5), 963-969 (2017).

[13] [13] Baba, H., Era, T., Ueyama, T., Tanaka, M., Development of high efficiency welding for thick plate steel using stabilized high current buried arc. *Welding* (ISSN 0043-2288), 60(5-6), 121-127 (2017) (in Croatian).

[14] [14] Perić, M., Garašić, I., Tonković, Z., Vuherer, T., Nižetić, S., Dedić-Jandrek, H., Numerical Prediction and Experimental Validation of Temperature and Residual Stress Distributions in Buried Arc Welded Thick Plates. *Int J Energy Res*, (2019) (in press).

[15] [15] Jeong, H., Park, K., Cho, J., Numerical analysis of variable polarity arc weld pool. *J Mech Sci Technol*, 30(9), 4307–4313 (2016).

[16] [16] Kollár, D., Kövesdi, B., Vigh, L.G., Horváth, S., Weld process model for simulating metal active gas welding. *Int J Manuf Technol*, (2019) (in press).

[17] [17] Perić, M., Tonković, Z., Garašić, I., Vuherer, T., An engineering approach for a T-joint fillet welding simulation using simplified material properties. *Ocean Eng*, 128, 13-21 (2016).

[18] [18] Perić, M., Tonković, Z., Rodić, A., Surjak, M., Garašić, I., Boras, I., Švaić, S., Numerical analysis and experimental investigation of welding residual stresses and distortions in a T-joint fillet weld. *Mater Des*, 53, 1052-1063 (2014).

[19] [19] Seleš, K., Perić, M., Tonković, Z., Numerical simulation of a welding process using a prescribed temperature approach. *J Const Steel Res*, 145, 49-57 (2018).

[20] [20] Abaqus 6.14-1, Dassault Systemes Simulia Corp., Providence, RI, USA, 2014.

Activities of the Croatian Academy of Engineering (HATZ) in 2018

Auspices, (Co) Organization of Conferences and Meetings of Public Interest

Auspice

1. Croatian Office for Creativity and Innovation (*HUKI*) – Workshop ("*IT Genious*", January 8 to 10, 2028, RIT Croatia, Zagreb Campus
2. Faculty of Architecture, Zagreb – Professional Conference – "Nearly Zero-Energy Buildings (NZEBs) by Connecting Science, Innovations and Economy", February 11, 2018
3. Faculty of Chemical Engineering and Technology – 12th Meeting of Young Chemical Engineers and Technologists, Zagreb, February 22, 2018
4. Faculty of Electrical Engineering and Computing – "*Brainhack Zagreb 2018*" as part of the event "Global Brainhack 2018", Zagreb, March 17 to 18, 2018
5. Faculty of Transport and Traffic Sciences – International Conference: Science and Traffic Development – ZIRP 2018 "*Transport and Logistics Industry in Digital Age*", Opatija, May 10 to 11, 2018
6. 5th International Conference on Road and Rail Infrastructure – CETRA 2018, Zadar, May 17 to 19, 2018
7. Faculty of Electrical Engineering and Computing – "*8th Congress of Alps Adria Acoustics Association*", Zagreb, FPZ, September20 – 21, 2018
8. Faculty of Textile Technology of Zagreb – International Scientific Conference "*9th ITC&DC 2018 – Magic World of Textiles*", IUC Dubrovnik, October 7 – 10, 2018
9. Faculty of Civil Engineering – International Conference "*RILEM International Conference on Sustainable Materials, Systems and Structures*", Rovinj, March 18-22, 2018
10. Croatian Color Society, TTF, GF, AF – International Color Day 2018, Zagreb, Technical Museum "Nikola Tesla", March 21, 2018
11. Croatian Association of Information and Communication Technology, Electronics and Microelectronics – Round Table "Industry 4.0 and Education", Opatija, May 21 – 25, 2018
12. HDKI, HKD – "26th Croatian Conference of Chemists and Chemical Engineers", Šibenik, April 9 to 12, 2018
13. Faculty of Agrobiotechnical Sciences Osijek – "1st International Student GREEN Conference", Osijek, May 17 – 18, 2018
14. Faculty of Electrical Engineering and Computing – "Conference on Research and Development in the ICT Field in Croatia" Zagreb, April 4, 2018
15. Faculty of Food Technology Osijek – International Scientific and Professional Conference "17th Ružička Days", Vukovar, September 19 to 21, 2018
16. Faculty of Chemistry and Technology in Split – 11th International Scientific and Professional Conference "With Food to Health", Split, October 28 to 29, 2018
17. Faculty of Mechanical Engineering and Naval Architecture – International Scientific Conference "*MOTSP 2018 – Management of technology – Step to sustainable production",* Primošten, June 06 to 08, 2018
18. University of Applied Sciences Velika Gorica – "4th Optometric Conference of Central and South-Eastern Europe (OCCSEE & EAOO) 2018", Pula, May 22 to 13, 2018
19. University of Applied Sciences Velika Gorica – Conference "Crisis Management Days", Brijuni, May 23 to 24, 2018
20. Faculty of Transport and Traffic Sciences – International Conference "ERGONOMICS 2018 – Emphasis on Wellbeing" Zadar, June 13 – 16, 2018
21. Croatian Energy Society – Hrvoje Požar Foundation Awards and Scholarships Ceremony, Hall of the Croatian Academy of Sciences and Arts, Zagreb, July 5, 2018
22. State Geodetic Administration, the Croatian Cartographic Society and the Faculty of Geodesy of the University of Zagreb – *14th International Conference on Geoinformation and Cartography*, Zagreb September 27-29, 2018
23. Croatian Energy Association – 27th Forum: Energy Day in Croatia, November 16, 2018
24. Center of Research Excellence for Data Science and Advanced Cooperative Systems, Research Unit for Data Science – *The Summer School 3rd Int'l Summer School on Data Science*, September 24-28, 2018 in Split, Croatia

25. Center of Research Excellence for Data Science and Advanced Cooperative Systems, Research Unit for Data Science – *3rd Int'l Workshop on Data Science,* Faculty of Electrical Engineering and Computing in Zagreb, October 16, 2018

26. Center for Computer Vision of the University of Zagreb – Annual Workshop *7th Croatian Computer Vision Workshop,* October 24, 2018, Zagreb, Croatia

27. Faculty of Electrical Engineering and Computing – Scientific and Professional Conference "New Research Activities at the Faculty of Electrical Engineering and Computing", Zagreb, October 15, 2018

28. Faculty of Food Technology and Biotechnology, Zagreb – Congress "*9th International Congress of Food Technologists, Biotechnologists and Nutritionists",* Zagreb, Hotel International, October 3 – 5, 2018

29. ELMAR Society and Faculty of Electrical Engineering and Computing – Symposium "*60th International Symposium ELMAR-2018"*, Zadar, September 16 – 19, 2018

(Co) Organization of Conferences

1. Faculty of Mechanical Engineering and Naval Architecture – Lecture "Discovery and Measurement of Higgs Boson Properties", Faculty of Mechanical Engineering and Naval Architecture, Zagreb, January 30, 2018

2. AMAC FER – Alumni FER: Lecture "Robotics Changes Industry and Society – Opportunities and Risks", Faculty of Electrical Engineering and Computing, February 14, 2018, Zagreb

3. Croatian Academy of Legal Sciences – Joint 10th (8) session of the Council and Coordination of AMZH, HATZ, APZH and AŠZ, Zagreb, February 22, 2018

4. HIS, HATZ and Faculty of Civil Engineering – Croatian Engineer's Day, Zagreb, Faculty of Civil Engineering, March 2, 2018

5. AMAC FER – Alumni FER: Lecture "Formal Methods – Myths and Reality", Faculty of Electrical Engineering and Computing, March 14, 2018, Zagreb

6. Department of Transport of the Croatian Academy of Engineering, Faculty of Transport and Traffic Science in Zagreb and Faculty of Tourism and Hospitality Management in Opatija – Round Table "Mobility Management – the Way to a Competitive Tourist Destination", Faculty of Tourism and Hospitality Management in Opatija, March 15, 2018

7. Department of Graphical Engineering of the Croatian Academy of Engineering and Center of Graphical Engineering – International Scientific Conference "Printing and Design", Školska knjiga, Zagreb, March 16, 2018

8. Department of Mining and Metallurgy of the Croatian Academy of Engineering and Faculty of Mining, Geology and Petroleum Engineering, Lecture: "Discovering Hot Water: Why is Geothermal Energy a Winning Card for Croatian Energetics", Faculty of Mining, Geology and Petroleum Engineering, March 26, 2018

9. Faculty of Mechanical Engineering and Naval Architecture, Zagreb, Lecture: History of Equations of Mathematical Physics : From Newton's Axioms to the Principle of Symmetry

10. Department of Mining and Metallurgy of the Croatian Academy of Engineering – Lecture "MIN-GUIDE Project and Mineral Resources Management Strategy in the EU", Faculty of Mining, Geology and Petroleum Engineering, April 9, 2018

11. University of Zagreb – Public Discussion: "Collaboration between Universities and Economy – Example of Good Practice", Assembly Hall of the University, April 11, 2018

12. AMAC FER – Alumni FER: Lecture: "Applications of Contemporary Technologies in Medicine", Faculty of Electrical Engineering and Computing, April 11, 2018

13. Committee for Economic and Regional Cooperation of the Croatian Academy of Egnineering, Croatian Chamber of Economy and Inovation Center Nikola Tesla – Round Table: "Kibernetic Physical Systems and Internet Things", Croatian Chamber of Economy, April 11, 2018

14. ATI, Croatian Waters – "1st International Water Congress – H_2O Summit", Rovinj, April 18 – 21, 2018

15. General Assembly (33rd Annual – Elective Assembly) on the occasion of the 25th Anniversary of the Academy, Zagreb, Old City Hall, Zagreb, May 21, 2018

16. Banquet organized by the Croatian Academy of Engineering, Dverce Palace, Zagreb

17. ANIU – 2018 CAETS Convocation – *Engineering a Better World: Sustainable Development of Agricultural and Forestry Systems*, Uruguay, Montevideo, September11-14, 2018

18. University of Zagreb Faculty of Forestry, Biotechnical Faculty, University of Ljubljana, Faculty of Forestry and Wood Sciences, Czech University of Life Science Prague, Forest Products Society and Innova Wood – 29th International Scientific Conference ICWST, Faculty of Forestry, Zagreb, December 6-7, 2018

19. Faculty of Forestry in Zagreb – International Scientific Conference "Position and Perspectives of Forestry and Wood Technology in the 21st Century", October 19, 2018

20. Department of Bioprocess Engineering of the Croatian Academy of Engineering – Symposium Biotechnology in Croatia "Vera Johanides" Zagreb, October 4, 2018

21. Department of Communication Systems of the Croatian Academy of Engineering – Lecture: "*Smart Phones, Medical Wireless Communications Inventions, Patents, Motivation, Challenges, Goals and Dreams of an Engineer*" and "*What butterflies and FBG sensors have in common and why PICs made Iphone X so expensive*", Faculty of Electrical Engineering and Computing, Zagreb, October 29, 2018

22. Department of Chemical Engineering of the Croatian Academy of Engineering – Lecture: "The Importance of Engineering Knowledge and Skills in Designing Innovative Products", Assembly Hall of the Croatian Academy of Sciences and Arts in Zagreb, November 9, 2018

Participation at the Meeting of Public Interest

1. AMAC FER – Alumni FER: Lecture "Human Hearing – A Perfect Information Channel ?", Faculty of Electrical Engineering and Computing, January 17, 2018

2. Croatian Chamber of Mechanical Engineers – Christmas-New Year's Party HKIS, Revival Hall of the National Hall of the Croatian Academy of Sciences and Arts, Zagreb, January 19, 2018

3. Faculty of Textile Technology in Zagreb, Faculty Day and Ceremonial Session, January 25, 2018

4. Academy of Medical Sciences of Croatia, Public Discussion "Surgical Treatment of Obstetrical Bleeding – from Ectomy to Condom", Great Hall of the Croatian Medical Association in Zagreb, January 30, 2018

5. Faculty of Civil Engineering – Ceremonial Session on the occasion of marking the Faculty Day, February 21, 2018

6. Faculty of Architecture of Zagreb – Professional Conference "Nearly Zero-Energy Buildings (NZEBs) by Connecting Science, Innovations and Economy", February 22, 2018

7. Faculty of Chemical Engineering and Technology – 12th Meeting of Young Chemical Engineers and Technologists, Zagreb, February 22, 2018

8. Academy of Medical Sciences of Croatia – Public Discussion "International Criminal Law – from Utopia to Dystopia", Large Lecture Hall of the Croatian Medical Association, February 27, 2018

9. Academy of Medical Sciences of Croatia- Round Table – "News on Proper Nutrition in Health Care", Large Lecture Hall of the Croatian Medical Association, March 20, 2018

10. Academy of Medical Sciences of Croatia – Public Discussion "Genomics and Personalized or Precise Medicine", Large Lecture Hall of the Croatian Medical Association in Zagreb, March 27, 2018

11. Croatian Academy of Sciences and Arts – "7th Oncology Colloquium of The Croatian Academy of Sciences and Arts", Library Hall of the Croatian Academy of Sciences and Arts, April 6, 2018

12. Annual Award Ceremony of the Society to young scientists and artists for 2017, Society of University Teachers and Other Scientists, Zagreb, April 12, 2018

13. Academy of Medical Sciences of Croatia – Public Discussion "Life Style and Brain Health – the Latest Scientific Knowledge", Large Lecture Hall of the Croatian Medical Association, Zagreb, April 24, 2018

14. Croatian Academy of Sciences and Arts – Ceremonial Session on the occasion of the Academy Day, April 26, 2018

15. AMAC FER – Alumni FER: Lecture "Deidentification – Privacy Protection in Multimedia Content" , Faculty of Electrical Engineering and Computing, May 16, 2018

16. Faculty of Graphic Arts – Ceremonial Session of the Faculty Council on the occasion of marking the Faculty Day, May 23, 2018

17. Department of Power Systems of the Croatian Academy of Engineering and Croatian Nuclear Society – Lecture " The Role of Nuclear Energy in Sustainable Development and Synergies with Renewable Sources ", Faculty of Electrical Engineering and Computing, May 23, 2018

18. Department of Power Systems of the Croatian Academy of Engineering and Croatian Nuclear Society – Lecture " The Role of Nuclear Energy in Sustainable Development and Synergies with Renewable Sources ", May 28, 2018

19. Academy of Medical Sciences – Public Discussion "Psychiatry today" Large Lecture Hall of the Croatian Medical Association, Zagreb, May 29, 2018

20. Marking the International Day of the Sava River – HAVK MLADOST, June 1, 2018

21. Croatian Chamber of Engineers Day – Opatija, Congress Hall (Ambassador Hotel), June 14, 2018

22. Round Table "Truths and Misconceptions About Higher Education Reform"- Assembly Hall of the Croatian Academy of Sciences and Arts, June 28, 2018

23. Faculty of Civil Engineering – Lecture: "Application of Satellitte Radar Interfeometry for Tracking of Displacement and Deformation from Field Displacement to Larger Spatial Coverage to Displacement on Isolated Housing Objects", September 21, 2018

24. Palace of the Croatian Academy of Sciences and Arts – Scientific Conference "Models of the Croatian Economy Development", September 25, 2018

25. Academy of Medical Sciences of Croatia – Public Discussion "Contemporary Endoscopic Diagnosis and Gastrointestinal Therapy Therapy", Large Lecture Hall of the Croatian Medical Association of Zagreb, September 25, 2018

26. Academy of Engineering Sciences of Serbia – Ceremonial Assembly, Ceremonial Hall of the Faculty of Civil Engineering of Belgrade, September 26, 2018

27. Croatian Academy of Sciences and Arts in Bosnia and Herzegovina – Round Table " Cooperation between Science and Economy as the Basis for Strengthening Competitiveness" and signing the Cooperation Agreement, Mepas Hotel, Mostar, October 3, 2018

28. Faculty of Transport and Traffic Sciences – Borongaj Science and Education Campus, October 9, 2018

29. Croatian Chamber of Economy – Round Table "Biomedical Engineering Development Trends", Zagreb, October 10, 2018

30. Faculty of Forestry – Celebration of the 120th Anneversary of the Foundation of the Faculty of Forestry of the University of Zagreb, October 18, 2018

31. Three Seas Initiative Forum – Towards a Digital Future, Croatian Chamber of Economy, Zagreb, October 23, 2018

32. Academy of Medical Sciences of Croatia – Round Table "Contemporary Treatment of Supraved Hydradynthesis", Large Lecture Hall of the Croatian Medical Association, Zagreb, October 30, 2018

33. Croatian National Theater – Ceremonial Marking of the Beginning of the 350th Anniversary of the Academic Year of the University of Zagreb and Ceremonial Session of the Senate on the occasion of marking the Day of the University of Zagreb, November 3, 2018

34. Croatian Academy of Sciences and Arts – Assembly of the Scientific Council for Technological Development, Academy Palace, November 7, 2018

35. Faculty of Civil Engineering – Opening the International Interdisciplinary Three-Day Conference "11th Days of Passive House in Croatia" , Great Hall, November 9, 2018

36. Croatian Energy Association – 27th Forum: "Energy Days in Croatia", Museum of Contemporary Art, November 16, 2018

37. Faculty of Mechanical Engineering and Naval Architecture – Ceremonial Session of the Faculty Council on the occasion of the Faculty Day, Zagreb, November 16, 2018

38. Rectorate of the University of Zagreb – 4th Session of the Commission for Development and Institutional Design of the System of Science and Higher Education. November 19, 2018

39. Faculty of Electrical Engineering and Computing – Faculty Day, Zagreb, November 23, 2018

40. Academy of Medical Sciences of Croatia – Round Table "Biosafety and Bioprotection". Large Lecture Hall of the Croatian Medical Association, Zagreb, November 27, 2018

41. Zagreb University of Applied Sciences – Ceremonial Session, Great Hall of the Mimara Museum, November 29, 2018

42. Conference "Croatia on the Sava" – Zagreb, Esplanade Hotel, Emerald Hall, December 3, 2018

43. Faculty of Mining, Geology and Petroleum Engineering of Zagreb – Ceremonial Session, Large Lecture Hall of the Faculty, December 8, 2018

44. Embassy of the State of Israel to the Republic of Croatia, Holiday Gathering and Farewell Ceremony with a party, Great Hall of the Palace of the Croatian Academy of Sciences and Arts, December 7, 2018

45. Presentation of the 1st Volume of the Croatian Technical Encyclopedia – Assembly Hall of the Rectorate of the University of Zagreb, December 10, 2018

46. Academy of Medical Sciences of Croatia – Public Discussion "Dies Academicus", Large Lecture Hall of the Croatian Medical Association Zagreb, December 12, 2018

47. Croatian Wood Cluster – Festive Banquet, Westin Hotel, December 12, 2018

48. Croatian Academy of Sciences and Arts – Holiday Reception, Academy Palace, December 13, 2018

49. Faculty of Geodesy – Lecture "Impressions from China", Faculty Council Hall, Zagreb, December 14, 2018

50. Society of University Teachers and Other Scientists – Christmas and New Year Congratulations, December 18, 2018

51. Faculty of Civil Engineering – Christmas Banquet, Zagreb, December 19, 2018

52. Faculty of Food Technology and Biotechnology – Traditional Christmas and New Year Congratulations, December 19, 2018

53. Faculty of Geotechnical Engineering – Ceremonial Session, December 20, 2018, Great Hall of GFV, Varaždin

HATZ Publications in 2018

1. *"Annual 2017-2018 of the Croatian Academy of Engineering"*, HATZ, Zagreb, 2018.

2. HATZ Bulletin in English *"Engineering Power" Vol. 12(3) 2017* (single issue)

3. HATZ Bulletin in English *"Engineering Power" Vol. 13(1) 2018* (single issue)

4. HATZ Bulletin in English *"Engineering Power"Vol.13 (2)2018* (single issue)

5. HATZ Bulletin in English "Engineering Power" *Vol. Vol.13 (3)2018* (single issue)

6. Book "*Life and inventions of Faust Vrančić*" (monograph, 3. expanded and edited edition), HATZ, POUZ, Zagreb, 2018. Prof. dr. sc. Gojko Nikolić

HATZ Activities Editor
Renata Budanec, Clerk for general and legal affairs
of the Croatian Academy of Engineering

Engineering Power – *Bulletin of the Croatian Academy of Engineering* Vol. 14(1) 2019 – ISSN 1331-7210
Publisher: Croatian Academy of Engineering (HATZ), 28 Kačić Street, P.O. Box 59, HR-10001 Zagreb, Republic of Croatia
Editor-in-Chief: Prof. Vladimir Andročec, Ph.D., President of the Academy retired Full Professor with tenure, University of Zagreb, Faculty of Civil Engineering
Editor: Prof. Zdravko Terze, Ph.D., Vice-President of the Academy University of Zagreb, Faculty of Mechanical Engineering and Naval Architecture
Guest-Editor: Zdenko Tonković, University of Zagreb, Faculty of Mechanical Engineering and Naval Architecture
Activities Editor: Renata Budanec
Editorial Board: Prof. Vladimir Andročec, Ph.D., Prof. Zdravko Terze, Ph.D., Prof. Slavko Krajcar, Ph.D.
Editorial Board Address: Croatian Academy of Engineering (HATZ), "Engineering Power" – Bulletin of the Croatian Academy of Engineering, Editorial Board, 28 Kačić Street, P.O. Box 59, HR-10001 Zagreb, Republic of Croatia
E-mail: hatz@hatz.hr
Graphical and Technical Editor: Vladimir Pavlić, Dipl. Eng. (GRAPA, Ltd., Zagreb) *Press:* Tiskara Zelina, Ltd., Zelina
Proof-reader: Miroslav Horvatić, MA *Circulation:* 250